massDOT
Massachusetts Department of Transportation

August 2024
Report No. 24-058

Feasibility of 3D Printing Applications for Highway Infrastructure Construction and Maintenance

Principal Investigator (s)
Simos Gerasimidis
Wen Chen
John Hart
Haden Quinlan

University of Massachusetts Amherst
Massachusetts Institute of Technology

Research and Technology Transfer Section
MassDOT Office of Transportation Planning

U.S. Department of Transportation
Federal Highway Administration

[This blank, unnumbered page will be the back of your front cover]

Technical Report Document Page

1. Report No. 24-058	2. Government Accession No.	3. Recipient's Catalog No.
4. Title and Subtitle Feasibility of 3D Printing Applications for Highway Infrastructure Construction and Maintenance		5. Report Date August 2024 6. Performing Organization Code 24-058
7. Author(s) B. D. Schagen, S. Zhang, J. A. Hart, W. Chen, H. E. Quinlan, S. Gerasimidis		8. Performing Organization Report No.
9. Performing Organization Name and Address University of Massachusetts Amherst, UMass Transportation Center, 130 Natural Resources Way, Amherst, MA 01003 Massachusetts Institute of Technology		10. Work Unit No. (TRAIS) 11. Contract or Grant No.
12. Sponsoring Agency Name and Address Massachusetts Department of Transportation Office of Transportation Planning Ten Park Plaza, Suite 4150, Boston, MA 02116		13. Type of Report and Period Covered Final Report - August 2024 (June 2022–August 2024) 14. Sponsoring Agency Code n/a
15. Supplementary Notes Project Champion - Catherine Chen, MassDOT		

16. Abstract

In recent years there has been a significant increase of interest in additive manufacturing (AM; also frequently referred to as 3D printing), yet AM is largely unexplored within infrastructure projects. By harnessing the new capabilities of AM, researchers have managed to access unprecedented new design capabilities and operational flexibility (e.g., on-demand, tool-free production). This revolutionary progress, however, has not been reflected in applications focused on civil or transportation infrastructure. This project explores AM innovations and their capabilities related to transportation infrastructure and as a potential future resource to assist MassDOT Highway Division's ongoing rehabilitation of bridge, tunnel, and highway structures, as well as classic recurring maintenance activities. The project's main research objective is to connect the additive manufacturing research community with MassDOT to explore additive repair techniques for corroded steel bridge beam ends.

17. Key Word 3D printing, transportation infrastructure, additive repair techniques, individual component manufacturing	18. Distribution Statement		
19. Security Classif. (of this report) unclassified	20. Security Classif. (of this page) unclassified	21. No. of Pages 74	22. Price n/a

Form DOT F 1700.7 (8-72) Reproduction of completed page authorized

This page left blank intentionally.

Feasibility of 3D Printing Applications for Highway Infrastructure Construction and Maintenance

Final Report

Prepared By:

Brian Dylan Schagen
PhD student, UMass

Shengbiao Zhang
PhD student, UMass

Wen Chen, Assistant Professor
UMass Amherst

Simos Gerasimidis
Associate Professor, UMass Amherst

Anastasios John Hart
Head of department Mechanical Engineering, MIT

Haden Edward Quinlan
Senior program manager, MIT

Prepared For:

Massachusetts Department of Transportation
Office of Transportation Planning
Ten Park Plaza, Suite 4150
Boston, MA 02116

Project Champion/Technical Representative
Catherine-Hong Chen, Sr. Structural Engineer
MassDOT

August 2024

This page left blank intentionally.

Acknowledgments

Prepared in cooperation with the Massachusetts Department of Transportation, Office of Transportation Planning, and the United States Department of Transportation, Federal Highway Administration.

The Project Team would like to acknowledge the efforts of Catherine-Hong Chen for her efforts to support the project and Mark Gauthier for his continuous lab support throughout the project.

Disclaimer

This page left blank intentionally.

Executive Summary

This study of Feasibility of 3D Printing Applications for Highway Infrastructure Construction and Maintenance was undertaken as part of the Massachusetts Department of Transportation (MassDOT) Research Program. This program is funded with Federal Highway Administration (FHWA) State Planning and Research (SPR) funds. Through this program, applied research is conducted on topics of importance to the Commonwealth of Massachusetts transportation agencies.

In this report, additive manufacturing methods are explored such as wire feed plasma arc additive manufacturing (PAAM) and cold spray additive manufacturing (CSAM) for repairing corroded bridge beams. Similar to the LENS repair investigation in a previous report, the focus in this report will be on experimenting with additive repair techniques for damaged construction materials and structures using PAAM and CSAM. The initial target will be A36 steel bridge beams, serving as a representative construction material to assess the feasibility and cost-effectiveness of PAAM and CS additive repairs.

CSAM, another additive manufacturing technology is explored in this report, which is a solid-state technique developed in the mid-1980s. Unlike methods involving melting, CS does not melt the powder feedstock during deposition, minimizing oxidation, thermal residual stresses, and phase transformations in the deposits. This makes CS suitable for depositing a wide range of metallic materials, including pure metals, commercial alloys, metallic glasses, and high-entropy alloys. In the CS process, compressed and preheated gas accelerates solid metal powders to high velocities, impacting them onto a substrate and ensuring metallurgical bonding.

The success of the additive repair is evaluated through numerical analysis and mechanical testing. Uniaxial testing is conducted on the repaired specimen in both compression and tension. From there, specimens are prepared and tested using pure A36 material, pure repair material, and finally the composite of both. The quality of the deposited material is carefully understood through microscopy scans. Finally, a study is performed to assess the economic feasibility of cold spray through an activity-based costing (ABC) model. This is a well-known method that can be used for calculating the costs of a given manufacturing task. Based on the elements of an exercise in the form of a series, that is, individual, discrete, and unique element, the costs can be allocated. In this case, we can think of materials, labor, equipment, and overhead that are applicable to include in the cost estimation. By summing up all the elements, the cost estimate is made for the manufacturing process.

This page left blank intentionally.

Table of Contents

Technical Report Document Page 1
Feasibility of 3D Printing Applications for Highway Infrastructure Construction and Maintenance 3
Acknowledgments 5
Disclaimer 5
Executive Summary 7
Table of Contents 9
List of Tables 11
List of Figures 11
List of Acronyms 13
1.0 Introduction 1
1.1 Overview of the Work 1
1.2 Background 1
2.0 Research Methodology 5
2.1 Base Material A36 5
2.1.1 Beam Preparation 5
2.1.2 A36 Tensile Coupons 6
2.2 Plasma Arc Additive Manufacturing 8
2.3 Cold Spray Additive Manufacturing 12
2.3.1 Powder WIP-316L 13
2.3.2 Powder SS06 17
2.3.3 Powder SS07 17
2.3.4 Powder SS08 18
2.3.5 EDM process 18
3.0 Results 23
3.1 Base Material A36 23
3.2 Plasma Arc Additive Manufacturing 25
3.3 Cold Spray Additive Manufacturing 26
3.3.1 Powder WIP-316L 26
3.3.2 Powder SS06 28
3.3.3 Powder SS07 30
3.3.4 Powder SS08 33
3.3.5 Conclusion 35
4.0 Cost Analysis 37
4.1 Cost of Material 37
4.2 Cost of Labor 43
4.3 Cost of Equipment and Overhead 44
4.4 Total Cost of Spray 47
5.0 Implementation and Technology Transfer 49
5.1 Presented Report 49
5.2 Conference Proceedings 49
5.3 Webinars 49
5.4 Lab Tours MassDOT, MIT and UMass Amherst 50
6.0 Conclusions 53
7.0 References 55

This page left blank intentionally.

List of Tables

Table 2-1: Chosen PAAM processing parameters 11
Table 2-2: Cold spray processing parameters: WIP-BC1 and 316L stainless steel powders 14
Table 3-1: Compression pillar results of various CSAM powders 35
Table 3-2: Tensile dogbone results of various CSAM powders 35
Table 4-1: Cost scenarios 39
Table 4-2: Gas consumption costs 41
Table 4-3: Labor cost estimate 43
Table 4-4: Equipment and overhead costs 45
Table 4-5: Additional Process Costs 46

List of Figures

Figure 2-1: Steel plate extraction from A36 beam element 6
Figure 2-2: Steel specimen extraction by laser cutting 6
Figure 2-3: EDM to obtain tensile dogbones 7
Figure 2-4: Instron tensile coupon testing 7
Figure 2-5: PAAM lab setup 8
Figure 2-6: PAAM material deposition 9
Figure 2-7: Parameter study: current (A) 10
Figure 2-8: Parameter study: wire feed rate (mm/sec) 10
Figure 2-9: Parameter study: offset (mm) 10
Figure 2-10: Schematic overview high-pressure CSAM system 12
Figure 2-11: VRC Gen III at UMass Amherst 13
Figure 2-12: SEM micrograph of WIP-BC1 powder 14
Figure 2-13: Cold spray of powders onto a corroded A36 plate substrate 15
Figure 2-14: Schematic of compression of A36/316L composite 16
Figure 2-15: Micrographs of the deposition of WIP-BC1 and 316L stainless steel 16
Figure 2-16: Deposition strategy of SS06 powder 17
Figure 2-17: Deposited SS07 powder on substrate 17
Figure 2-18: Deposited SS07 powder on substrate 18
Figure 2-19: Thickness preparation of the A36 steel substrate 19
Figure 2-20: Final cutting and tensile coupons obtained with EDM 19
Figure 2-21: Tensile coupon obtained with EDM 20
Figure 2-22: Testing rig tension coupons and end result of a composite coupon 20
Figure 2-23: Testing rig for compression pillars 21
Figure 3-1: Stress-strain curve of A36 compression pillars under uniaxial compression 24
Figure 3-2: Stress-strain curve of A36 tension coupons under uniaxial tension 25
Figure 3-3: Stress-strain curve of PAAM coupons under uniaxial tension 26
Figure 3-4: Tensile tests of A36/316L composites. 27
Figure 3-5: Compressive tests of pure A36, pure 316L deposition, and A36/316L composites 28
Figure 3-6: Stress-strain curves of pure A36, pure SS06 deposition, and A36/SS06 composites 29
Figure 3-7: Stress-strain curves of pure A36, pure SS06 deposition, and A36/SS06 composites 30
Figure 3-8: Stress-strain curves of pure A36, pure SS07 deposition, and A36/SS07 composites 31
Figure 3-9: Stress-strain curves: pure A36 and pure SS07 deposition tension coupons 32
Figure 3-10: Stress-strain curves: pure A36 and composite A36/SS07 deposition tension coupons 32
Figure 3-11: Stress-strain curves: pure A36, pure SS08 deposition, and A36/SS08 composites 33
Figure 3-12: Stress-strain curves: pure A36 and pure SS08 deposition 34

Figure 3-13: Stress-strain curves: pure A36 and composite A36/SS08 34
Figure 4-1: Post-spray report using the GEN III system for SS08 powder deposition 40
Figure 4-2: Relative cost drivers at different DEs 42
Figure 5-1: Screenshots of given webinars 50
Figure 5-2: CSAM lab tour 51

List of Acronyms

Acronym	Expansion
ABC	Activity-based costing
CFRP	Carbon Fiber Reinforced Polymer
CSAM	Cold Spray Additive Manufacturing
DE	Deposition efficiency
EDM	Electric Discharge Machining
FHWA	Federal Highway Administration
MassDOT	Massachusetts Department of Transportation
PAAM	Plasma Arc Additive Manufacturing
RE	Reclamation efficiency

This page left blank intentionally.

1.0 Introduction

1.1 Overview of the Work

This study of Feasibility of 3D Printing Applications for Highway Infrastructure Construction and Maintenance was undertaken as part of the Massachusetts Department of Transportation (MassDOT) Research Program. This program is funded with Federal Highway Administration (FHWA) State Planning and Research (SPR) funds. Through this program, applied research is conducted on topics of importance to the Commonwealth of Massachusetts transportation agencies.

In recent years there has been a significantly increased interest in additive manufacturing (also frequently referred to as 3D Printing), a design platform largely unexplored within infrastructure projects. Recent progress in this field has been studied through a Phase 1 study that examined applications focused on transportation infrastructure, such as 3D-printed repairs to deteriorated steel bridge beam ends. This proposed project will build on the Phase 1 study and explore further the feasibility of 3D printing applications for highway construction and maintenance in the Commonwealth of Massachusetts.

The research effort will focus on the following objectives:

1. Explore the feasibility of additive repair technologies for real corroded steel beams ends. Different additive manufacturing solutions and repair technologies are examined in the lab and potentially on site.
2. Research the key factors related to the different repair technologies and equipment investigated that can impact the success of an attempted repair (e.g., velocity of material being deposited). Use the research to develop a list of suggested options for equipment and facilities that seem well suited for handling 3D printing applications and the associated qualifications testing of 3D printing repaired steel bridge beams.

1.2 Background

In a recent assessment, the infrastructure of the United States has been categorized as ranging from poor to fair condition, with numerous components nearing the end of their operational life span. Specifically addressing the state of the transportation network, out of more than 600,000 bridges listed in the National Bridge Inventory, 55,000 are identified as structurally deficient, with an estimated backlog of bridge rehabilitation needs totaling US$123 billion [1]. Among the various causes of structural deficiency [2], corrosion emerges as a significant issue affecting both reinforced concrete [3–5] and steel bridge structures [6].

Corrosion is largely attributed to the malfunctioning of deck expansion joints, which are continuously exposed to environmental and human-induced deterioration factors, accelerating their aging process. Consequently, these joints fail to effectively drain the water or deicing agents away from the bearing

area, where beams are supported. The water seepage often carries high concentrations of chemicals used seasonally for road winterization, leading to corrosion initiation, particularly in the bottom of the beam web. Prolonged exposure to such conditions can result in considerable thickness loss, directly compromising the load-bearing capacity of the bridge girders and, consequently, the overall structural integrity.

Beam end corrosion has been extensively studied in eastern Asia, particularly in Japan and Korea. Sugimoto et al. [10] examined a railway deck plate girder from the early twentieth century, proposing a method for assessing capacity reduction due to bending and shear failure at midspan and support areas, respectively. Kim et al. [11] conducted experiments on stiffened beams with artificially reduced thickness, finding that corrosion leads to larger shear failure regions. Ahn et al. [12] investigated the impact of pitting and corrosion hole damage, concluding that they significantly affect shear buckling behavior when reaching a critical corrosion level in the diagonal tension field. Khurram et al. [13] suggested using the minimum thickness within any damaged height to simulate corrosion damage in computational analysis.

Various repair techniques for corroded girders have been explored. For instance, Ahn et al. [14] suggested using CFRP due to its light weight, high strength, and easy application. Miyashita et al. [15] using the same method performed shear buckling tests on intact, damaged, and repaired specimens using CFRP, noting a recovery of load carrying capacity in the repaired beam. Ogami et al. [16] applied studs and rebar to corroded girders before covering it with resin, preventing buckling under axial compressive loading. Wu et al. [17] experimentally highlighted the impact of web section loss, which results in a significant ultimate load decrease. However, this phenomenon is mainly related to the web corrosion within the flange diffusion range. In a second study the specimens were strengthened by welding stiffeners on the two sides of the web and partially encasing it with high-strength grout [18].

Furthermore, in collaboration with MassDOT, research is performed at UMass Amherst on unstiffened deteriorated steel beams. With that, new loading procedures to accurately estimate their remaining strength are developed. Also, an analysis procedure is developed to understand the impact of corrosion on the corroded beams [19]. Furthermore, the study expands toward an experimental and numerical study on naturally corroded I-beams [20,21]. The current provisions are found to underestimate the capacity of beams. Moreover, the methodology is provided for improved failure loads for the current provisions. Second, a report is developed for MassDOT to communicate the research [22]. Third, to quantify the remaining capacity of bridge plate girders with naturally corroded beam ends, a computational and analytical formulation is performed and validated with experimental testing [23]. Moreover, 3D laser scanning technologies are evaluated to estimate capacity [24].

On the other hand, in a joint collaboration with MassDOT, MIT, and UMass Amherst, the future of corrosion repair is explored using additive manufacturing technologies (AM). Using AM technologies as repair could significantly reduce costs and time. Repairs are expected to be performed in minutes following our experience using the high-pressure cold spray system (GENIII, VRC Metal Systems). Several ideas such as laser DED, laser-engineered shaping, CSAM, and PAAM are identified as future candidates [25]. In a later study, laser DED is the first promising technology to be employed as structural repair [26].

At the University of Connecticut, Zmetra et al. [27] proposed welding shear studs to the web and

encasing the girder end in ultrahigh-performance concrete (UHPC), successfully restoring the girder's capacity in experiments. Push-out tests on studs embedded in UHPC were conducted to evaluate their capacity [28,29], with additional tests on specimens subjected to accelerated electrochemical corrosion to assess durability [30].

Researchers have tackled beam end corrosion from various angles, including residual bearing capacity evaluation and innovative repair techniques. Apart from Sugimoto et al.'s work on railway bridges and prior work by the authors [31], most efforts have introduced corrosion artificially as uniform thickness reduction on intact beams. However, naturally corroded beams for testing poses challenges due to the nonuniform deterioration phenomenon, which varies in topology and intensity, influenced by factors such as bridge age, exposure conditions, bearing type, and deck joint positions. Simulating corrosion as uniformly reduced thickness may yield unrealistic results in such complex real-world conditions [32].

Lately, there has been a surge in interest surrounding the beam corrosion issue, particularly sparked by recent endeavors in Massachusetts aimed at developing innovative repair techniques for deteriorated steel beam ends. This study serves as the experimental segment of a broader project, aiming to assess viable technologies for repairing corroded steel beam ends. What sets our methodology apart is its foundation in using real corroded beam elements. We conducted tests on naturally corroded specimens sourced from bridge demolition projects across Massachusetts. This report delves into the repair methods used and the effectiveness of each repair, and provides a comparative analysis, alongside detailed descriptions of individual specimens. We present measured data, failure modes, and mechanisms observed. Additionally, we evaluate the current procedures in accordance with ASTM standards. Moreover, the specimens were prepared in accordance with ASTM standard E8 (tension) and E9 (compression). It is concluded that the dimensions of the specimens were in accordance and match the requirements for the Instron 5569, that is used for testing. The findings detailed in this report serve as the groundwork for computational efforts aimed at enhancing current repair methodologies for corroded beam ends.

This page left blank intentionally.

2.0 Research Methodology

In this chapter, the research methodology is presented for obtaining results using different additive manufacturing technologies. At first, the A36 base material is discussed which has been generally used for the bridges that have been built in the United States. Additive manufacturing techniques such as PAAM and CSAM have been used as possible candidates for repair of steel corroded bridge beams. These technologies are cost and time efficient, precise, and environmentally friendly due to the material that can be saved [33,34].

Throughout the chapter a step-by-step guide is given on how specimens are obtained when applying the techniques described earlier. Electric discharge machining (EDM) is used to cut and obtain specimens according to the ASTM standards. From there the specimens are tested using an Instron 5569 system.

2.1 Base Material A36

In collaboration with MassDOT, bridge beams made of A36 structural steel from Orange, MA (reference no: O-03-009), have been disassembled and transported to the Brack lab at UMass Amherst for future research. Throughout the research, beams have been used for various research goals including the examination of different additive manufacturing techniques for 3D repair. A step-by-step approach is discussed in the next section.

2.1.1 Beam Preparation

An evenly corroded surface is selected to be used as substrate for the examination of different additive manufacturing techniques. A cutout section of this corroded part of the beam web 31.5 × 19.5 × 0.5 in. is obtained (Figure 2-1). The intact thickness of the web is 14.1 mm.

Figure 2-1: Steel plate extraction from A36 beam element

In Figure 2-2, precise A36 substrates are obtained using laser jet cutting. Each plate is 100 × 200 mm, which makes the plates suitable for further test purposes.

Figure 2-2: Steel specimen extraction by laser cutting

2.1.2 A36 Tensile Coupons

With the goal of restoring the strength and ductility of the repaired component, we study the repair of ASTM A36 steel by AM. Therefore, the mechanical properties of A36 are quantified by preparing and performing compression and tensile coupon tests. Using EDM, a 3 mm thick strip as shown in Figure 2-3 is obtained. From there, the tensile coupons are cut according to the ASTM standard dimensions as shown in Figure 2-4.

The tensile properties of the A36 specimens were examined at a quasi-static strain rate of 2×10^{-4}/s on an Instron 5569 system. A non-contact AVE2 laser extensometer with a displacement resolution of 0.5 μm was used to measure the strain. The extensometer reads two white dots that are manually applied on each specimen.

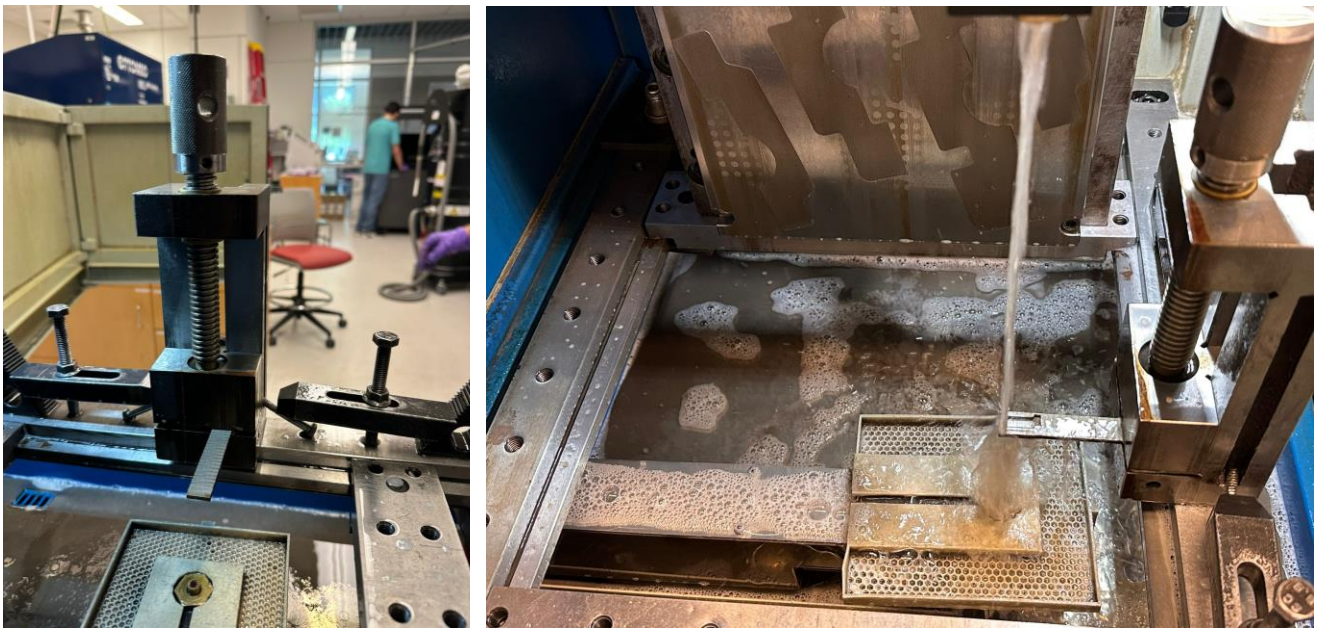

Figure 2-3: EDM to obtain tensile dogbones

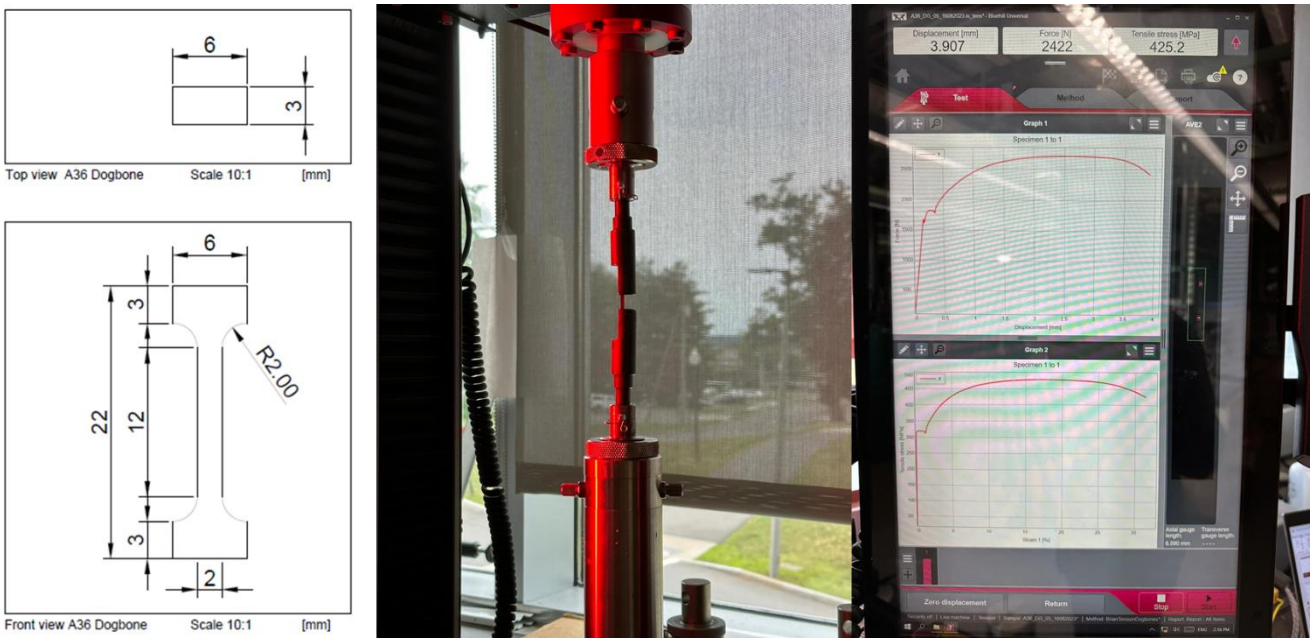

Figure 2-4: Instron tensile coupon testing

2.2 Plasma Arc Additive Manufacturing

One of the first methods discussed in this work is PAAM. This method has been widely used for manufacturing and repair. At UMass Amherst a PAAM setup is developed that consists out of the following parts:

- A conveyor for movement along the *x*-,*y*- and *z*-axes;
- The wire feed material and gas feeder; and
- The control panel for setting the print parameters, such as nozzle speed, wire feed rate, offset, and current.

In Figure 2-5 the PAAM lab setup is shown. Prior to printing, a substrate design is made where all single tracks are laid out on the substrate. Each single track is printed using a set of different parameters to understand the influence of each parameter.

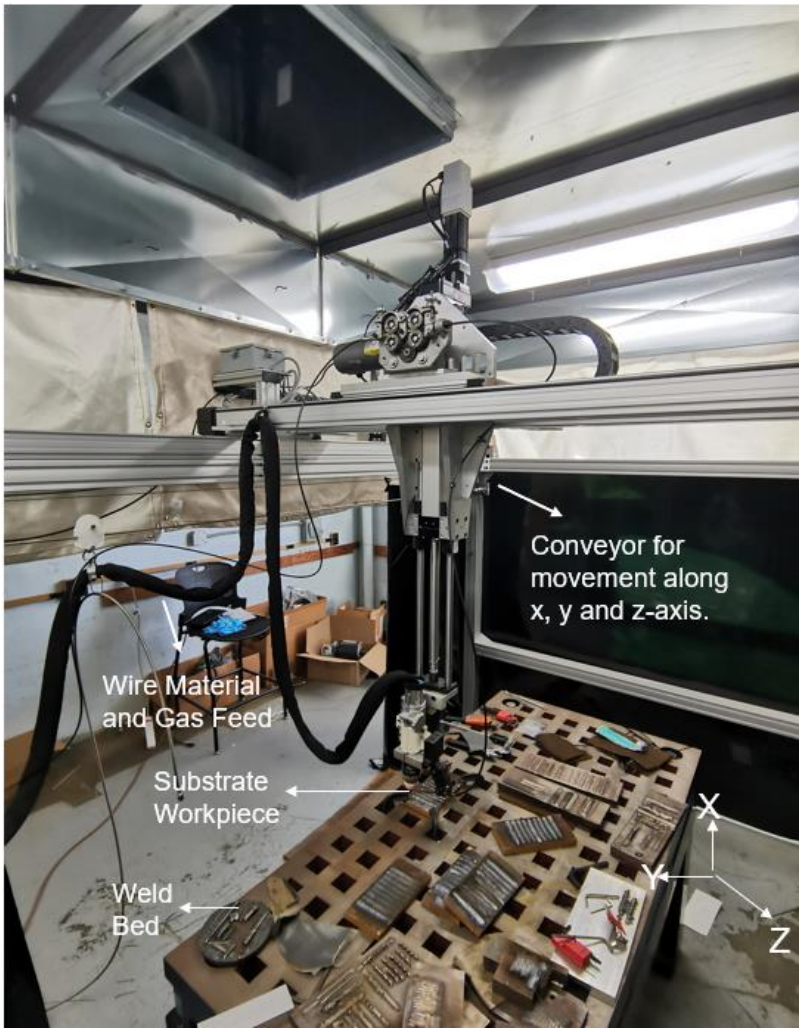

Figure 2-5: PAAM lab setup

An example of a parameter study is shown in Figure 2-6, where different currents are used. As shown, there is some difference in quality between each of the tracks. Some of the tracks are uneven or show discontinued deposition along the track. As a result, a selection is made on the print parameters of

nozzle speed, wire feed rate, offset, and current for the best quality. The tracks created with this set of parameters are then selected for further testing.

Figure 2-6: PAAM material deposition

As mentioned, a parameter study is performed by changing the following print parameters:

- Offset 2–18 mm,
- Wire feed rate 9–41 mm/sec,
- Current 100–325 A.

A nozzle speed of 4.75 mm/sec is selected to be a workable speed for the used equipment. The results of each of the parameter studies are shown in Figures 2-7 through 2-9. Some of the defects that are visible are pores or discontinuation of the tracks [35–46].

Parameters	Nozzle Speed (mm/sec)	Offset (mm)	Wire Feed Rate (mm/sec)	Current (A)
I	4.75	10	25	325
II				275
III				250
IV				225
V				200
VI				175
VII				150
VIII				125
IX				100

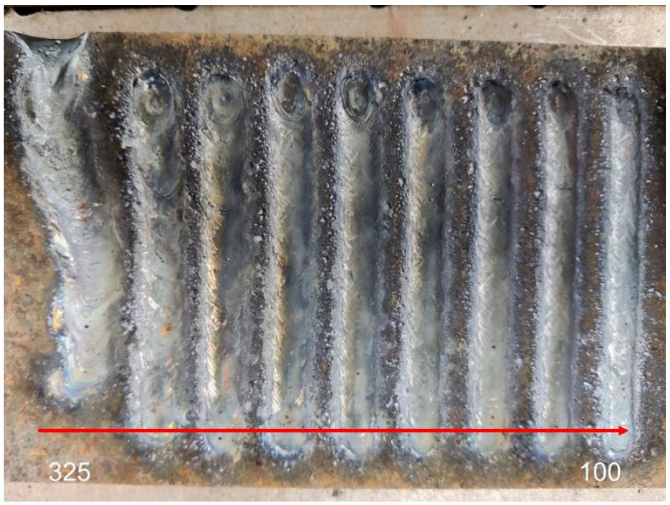

Figure 2-7: Parameter study: current (A)

Parameters	Nozzle Speed (mm/sec)	Offset (mm)	Current (A)	Wire Feed Rate (mm/sec)
I	4.75	10	200	9
II				13
III				17
IV				21
V				25
VI				29
VII				33
VIII				37
IX				41

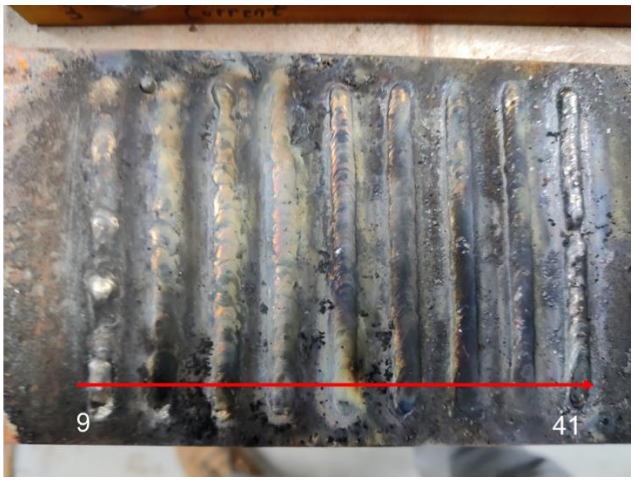

Figure 2-8: Parameter study: wire feed rate (mm/sec)

Parameters	Nozzle Speed (mm/sec)	Wire Feed Rate (mm/sec)	Current (A)	Offset (mm)
I	4.75	10	200	18
II				16
III				14
IV				12
V				10
VI				8
VII				6
VIII				4
IX				2

Figure 2-9: Parameter study: offset (mm)

An overview of the chosen PAAM processing parameters is given in Table 2-1. The parameters given in red (i.e., nozzle speed, offset, wire feed rate, and current of 200, 175, and 150 A) are the ones selected for future use and study of the mechanical properties. With that, the single tracks are performed in the lab, where only a slight change in current between 150 and 200 A is performed.

Table 2-1: Chosen PAAM processing parameters

	Effect of Current				Effect of Wire Feed Rate				Effect of Offset			
Parameters	Nozzle Speed (mm/sec)	Offset (mm)	Wire feed rate (mm/sec)	Current (A)	Nozzle Speed (mm/sec)	Offset (mm)	Current (A)	Wire feed rate (mm/sec)	Nozzle Speed (mm/sec)	Wire feed rate (mm/sec)	Current (A)	Offset (mm)
I				325				9				18
II				275				13				16
III				250				17				14
IV	**4.75**	**10**	**25**	225	4.75	10	200	21	4.75	10	200	12
V				**200**				25				10
VI				**175**				29				08
VII				**150**				33				06
VIII				125				37				04
IX				100				41				02

2.3 Cold Spray Additive Manufacturing

A possible repair method for corroded steel bridge beams is CSAM, where the substrate is being treated by an oxide-free deposit without damaging the underlying substrate thermally [47–61]. In this process, a high temperature compressed gas (nitrogen) is used to accelerate the metal powder feedstock, reaching all the way up to 300 m/s and beyond. With cold spray, it is possible for a bridge beam to retain its original capacity using targeted and limited added material. A so-called metallurgical bond is created between the substrate and the powder ensuring the ability to retain capacity.

In recent years, the use of CSAM applications has grown significantly due to the low working temperature, less product size limitations, and one order of magnitude higher deposition rates compared to other established additive manufacturing techniques. Furthermore, cold sprayed deposits provide effective protection against corrosion, high temperature, oxidation, erosion, and chemicals [33]. The current study discusses a new state-of-the-art application where CSAM is introduced for additive repair of corroded steel bridge beams.

A high-pressure cold spray system (>1 MPa) is one where compressed gas is divided into two streams upon entering the system. The propulsive gas enters through the gas heater, where it is heated to a high temperature (650°C). Simultaneously, a second stream is generated where the carrier gas passes through the powder feeder enabling the transfer of feedstock particles. Before entering the nozzle, the gases are mixed to generate a supersonic gas and powder stream [34]. For this to work, the pressure of the carrier gas must be slightly higher than the propulsive gas. It is worth noting that the high-velocity particles form a deposit or coating well below the melting temperature. Another system would be low pressure cold spray, but in general this system is only limited to deposition of copper and aluminum. In Figure 2-10, a schematic overview is given of such a high-pressure CSAM system. A high-pressure cold spray system, known as the VRC Gen III (VRC Metal Systems, SD, USA), was utilized in this project.

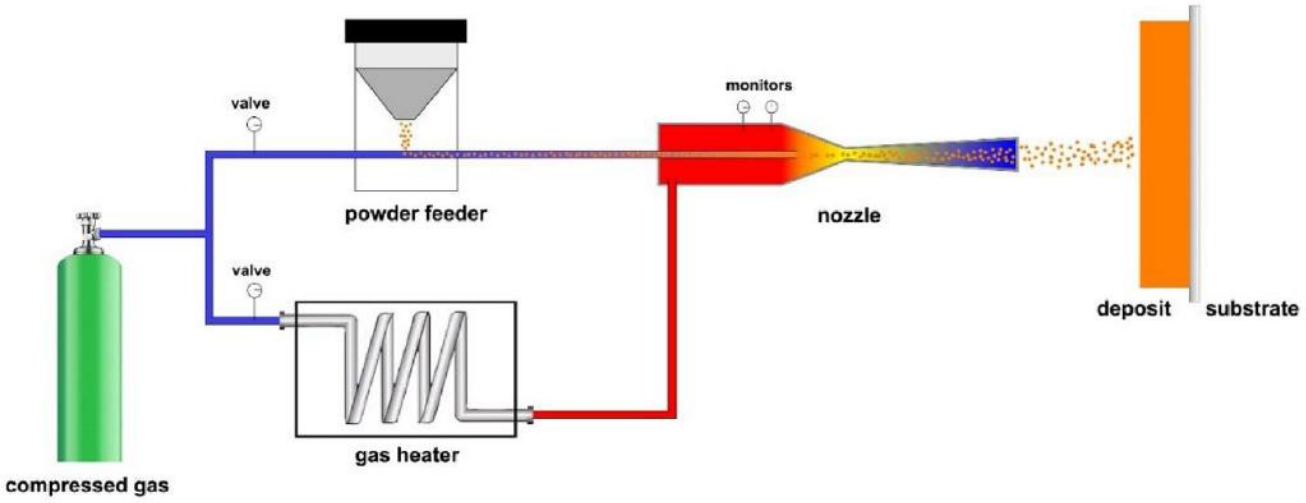

Figure 2-10: Schematic overview high-pressure CSAM system

In Figure 2-11, the VRC Gen III (VRC Metal Systems, SD, USA) system is shown. A concealed environment is created within the deposition chamber according to health precautions. During the cold spray process, the chamber is sealed and under constant air filtering. Besides that, a parameter sheet is prepared to operate the system and deposit with the desired printing parameters, such as pressure, temperature, nozzle speed, and the feed rate.

Figure 2-11: VRC Gen III at UMass Amherst

2.3.1 Powder WIP-316L

With the goal of restoring the strength and ductility of the repaired component, we study the repair of ASTM A36 steel by cold spray. Ideally, the same material (i.e., A36) should be used for the bridge beam repair for mechanical and electrochemical homogeneity across the repaired region. However, to our best knowledge, A36 spherical powders for cold spray are not commercially available, so we selected a dissimilar material of 316L stainless steel in this study. There are several merits of choosing 316L stainless steel as the filler material for the bridge beam repair. First, 316L stainless steel shows overall excellent corrosion resistance and mechanical properties compared to low-carbon steel. Second, extensive studies have been conducted on cold spray of 316L stainless steel, thus providing us with abundant references and database to understand its microstructure and properties. In addition, 316L stainless steel powders are cost-effective and readily available in the market. Finally, the powder form of many existing infrastructure materials may not be readily available for future cold spray repair and on the other hand customized powders are often too expensive.

Cold spray process procedure

Commercially available WIP-BC1 powder (provided by Solvus Global) and 316L stainless steel powder (provided by Powder Alloy Corporation) were utilized as the feedstock powder in the current research effort. Figure 2-12 captures the typical microparticle morphologies of the WIP-BC1 powder feedstock, which maintained an angular morphology alongside an average powder particle size of 64 µm. WIP-BC1 powder is based on chromium carbide and nickel, uses an optimized particle size distribution, and has a high fluidity. WIP-BC1 is designed to be cold sprayed as the first layer to appropriately prepare harder substrates for coatings. Therefore, before the surface was coated with 316L stainless steel powder, a thin layer of bond coat that consists of WIP-BC1 powder was applied on the surface. The 316L stainless steel powders have a particle size range of 15–43 µm. A high-pressure cold spray system, known as the VRC Gen III (VRC Metal Systems, SD, USA), was utilized in this project. The VRC Gen III cold spray system was equipped with a NZZL0082 tungsten carbide-cobalt nozzle to deposit a thin layer of WIP-BC1 powder and then multiple layers of the 316L stainless steel powder onto an A36 plate (Figure 2-13). The ASTM A36 low-carbon steel was taken from a corroded steel bridge in Massachusetts by EDM. Air, nitrogen (N_2), and helium (He) are three common carrier gases used in the cold spray process [47]. It has been shown that the type of carrier gas notably affects the feedstock particles' velocity. An increase in the particle velocity facilitates particle deformation and, subsequently, bonding. As a result, the quality of deposited material and deposition efficiency (DE) is enhanced due to the improved bonding. Among these carrier gases, it has been shown that He and N_2 gas provide the highest particle velocity compared to the other carrier gases. Considering that He is costly, N_2 is selected as the carrier gas. The cold spray processing parameters are summarized in Table 2-2.

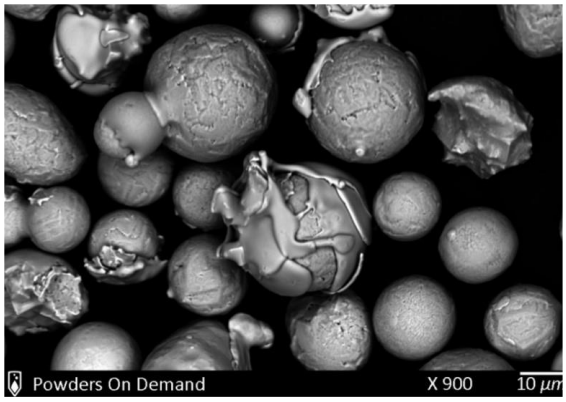

Figure 2-12: SEM micrograph of WIP-BC1 powder

Table 2-2: Cold spray processing parameters: WIP-BC1 and 316L stainless steel powders

Carrier gas	Gas temperature	Gas pressure	Spray angle	Standoff distance	Transverse speed
N_2	650°C	900 psi	90 degrees	25 mm	200 mm/s

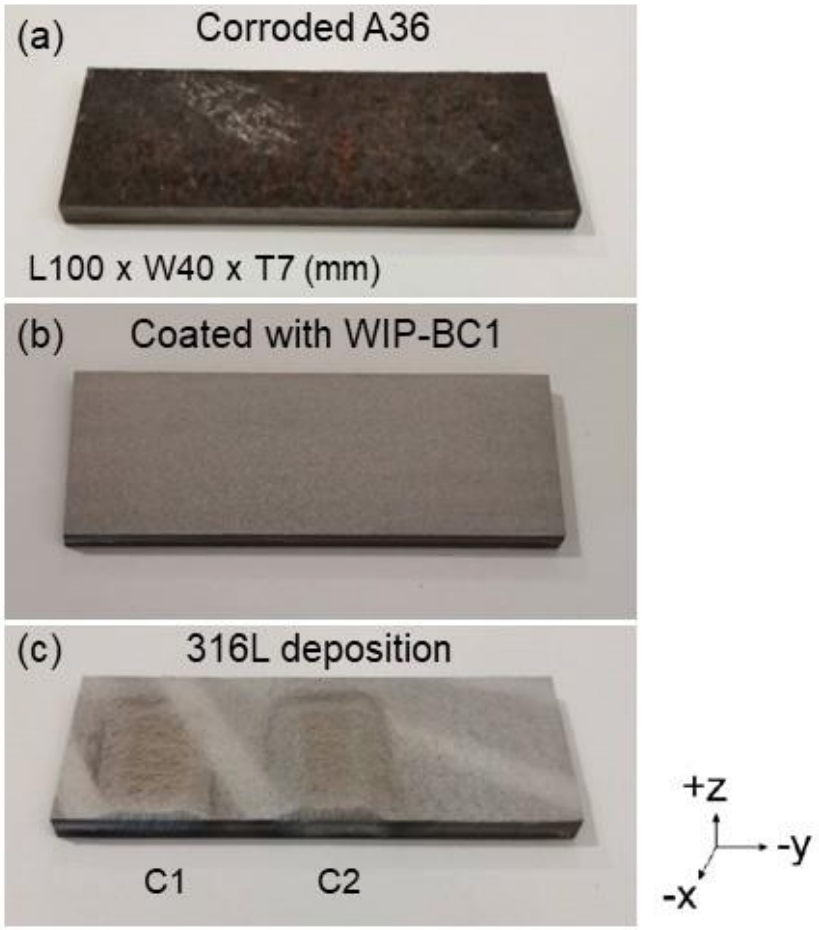

Figure 2-13: Cold spray of powders onto a corroded A36 plate substrate

After deposition of WIP-BC1 and 316L stainless steel, the microstructure was carefully analyzed by an Olympus BX51 optical microscope (OM). Samples were polished using SiC abrasive papers of 400, 800, and 1,200 grit, followed by colloidal silica suspension polishing. Dogbone-shaped tensile samples with the gauge section were cut from the plate by EDM. The gauge length, width, and thickness of the tensile specimens were 6.5, 2.0, and 1.2 mm, respectively. There are two types of dogbones: one only containing pure 316L stainless steel to examine the mechanical properties of the deposition itself, and the other consisting of half 316L stainless steel and half A36 with their interface along the width direction. The tensile properties of the specimens were examined at a quasi-static strain rate of 2×10^{-4}/s on an Instron 5569 system. A non-contact AVE2 laser extensometer with a displacement resolution of 0.5 μm was used to measure the strain. To study the compressive property after repairing by cold spray, uniaxial compression tests of pillars (pure A36, pure 316L stainless steel, and A36/316L composite) with dimensions of approximately 2 × 2 × 4 mm (height) were performed on the same Instron 5969 machine with a strain rate of 5×10^{-4}/s at room temperature. Two types of compression pillars are prepared with different interface orientations, one with A36/316L interface vertical during compression test, the other with A36/316L interface horizontal, as shown in Figure 2-14.

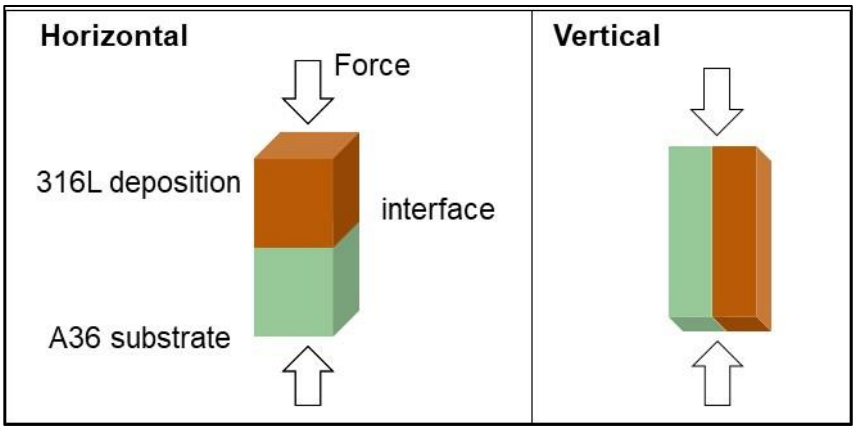

Figure 2-14: Schematic of compression of A36/316L composite

Cold spray results and discussion

Figure 2-15 shows the typical optical micrographs (OM) of the well-polished 316L stainless steel cross-sectional deposition onto as-corroded A36 surface with a thin layer of WIP-BC1. The addition of WIP-BC1 has been reported to have multiple effects—shot-peen, clean and roughen the surface, in addition to creating a thin layer of WIP-BC1 coating [48]. Dense deposition with a porosity less than 0.6% measured by ImageJ software has been achieved without observable defects such as delamination or cracking in the 316L deposit. The particles showed elongated shapes due to severe deformation during cold spray process.

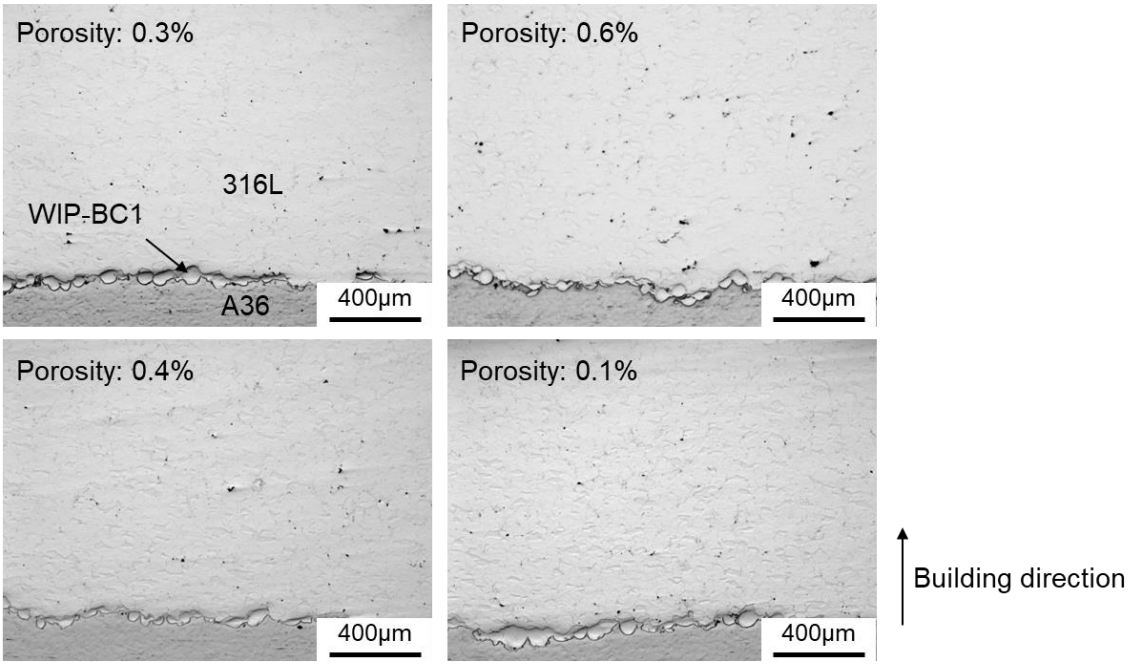

Figure 2-15: Micrographs of the deposition of WIP-BC1 and 316L stainless steel

2.3.2 Powder SS06

Besides WIP316L, a series of SS0X stainless steel powders have been proposed by VRC metal systems as possible repair powder, the first of which is SS06. VRC's SS06 powder is a blend of 400-series stainless steel with specially selected spherical ceramic constituents that help to achieve exceptional bond strength on hardened steel substrates. The powder size distribution is from 18.02 to 42.74 µm (D10: 18.02 µm; D25: 22.17 µm; D50: 29.00 µm; D75: 36.11 µm; and D90: 42.74 µm). Furthermore, the composition of the powder is prescribed as follows: Si: <1.5%; Cr: 45–48%; Fe: 42–44%; Mn: <1.5%; and C: 1.7–2.3%. Following the previous described process, an intermediate BC01 layer is applied, after which multiple layers of SS06 powder are performed to ensure a good bonding between the substrate and intermediate layers.

Figure 2-16: Deposition strategy of SS06 powder

2.3.3 Powder SS07

Besides SS06, the SS07 powder is selected as a possible powder candidate. The VRC's SS07 powder is a blend of 400-series stainless steel with specially selected spherical ceramic constituents that help to achieve better bond strength on hardened steel substrates. The powder size distribution is from 17.12 to 43.05 µm (D10: 17.12 µm; D25: 21.85 µm; D50: 28.55 µm; D75: 37.12 µm; and D90: 43.05 µm). Furthermore, the composition of the powder is prescribed as: Si: <1.5%; Cr: 63–76%; Fe: 21–23%; Mn: <1.5%; and C: 2.5–3.5%. The deposit rate for the SS07 powder increases from 17% to 34%, meaning a twofold efficiency of material deposited. There is a variation of thickness deposit on the substrate shown in Figure 2-17. This is explained by the back-and-forth movement of the robot.

Figure 2-17: Deposited SS07 powder on substrate

2.3.4 Powder SS08

Finally, the SS08 powder is considered, which is the cheapest of its kind. VRC's SS08 powder is a blend of 400-series stainless steel with specifically sized Ferrochrome constituents. The powder size distribution is from 15.09 to 47.33µm (D10: 15.09 µm; D25: 21.10 µm; D50: 29.96 µm; D75: 39.64 µm; and D90: 47.33 µm). Furthermore, the composition of the powder is prescribed as: Si: 0–1%; Cr: 39–43%; Fe: BAL; Mn: 0–1%; and C: 4–5%. Again, the deposit reached far higher deposit rates that were up more than 30%. In Figure 2-18, a track of deposited material is shown. Each layer is about 0.5 mm; depending on the thickness needed, the number of layers is determined. In this research, a thickness of 3 mm is sufficient due to testing dimension restrictions. Moreover, a thickness of 3 mm is used for the tensile coupons. The reason for this is that the tensile strength of the coupon needs to remain within capacity of the Instron 5569.

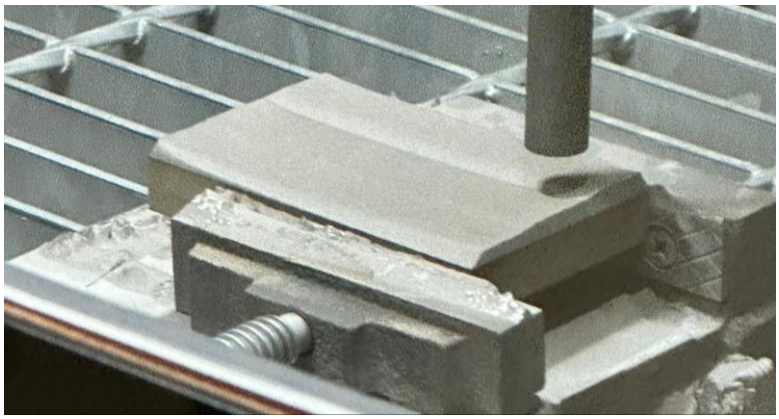

Figure 2-18: Deposited SS07 powder on substrate

2.3.5 EDM process

An electric discharge machining process is developed to obtain the test coupons. The A36 steel plate including the deposited cold spray material is clamped for precise cutting. The first step is to cut the plate completely through the thickness of the plate to obtain a smaller specimen. EDM cuts generally take long, so it is recommended to have shorter cuts if possible. Second, the smaller substrate is sliced through the *z*-plane to create the desired length. In this case, the goal is to have 1.5 mm of A36 steel so both composite test and pure cold spray material coupons are obtained. In Figure 2-19, the thickness preparation of the substrate is shown for the first two steps.

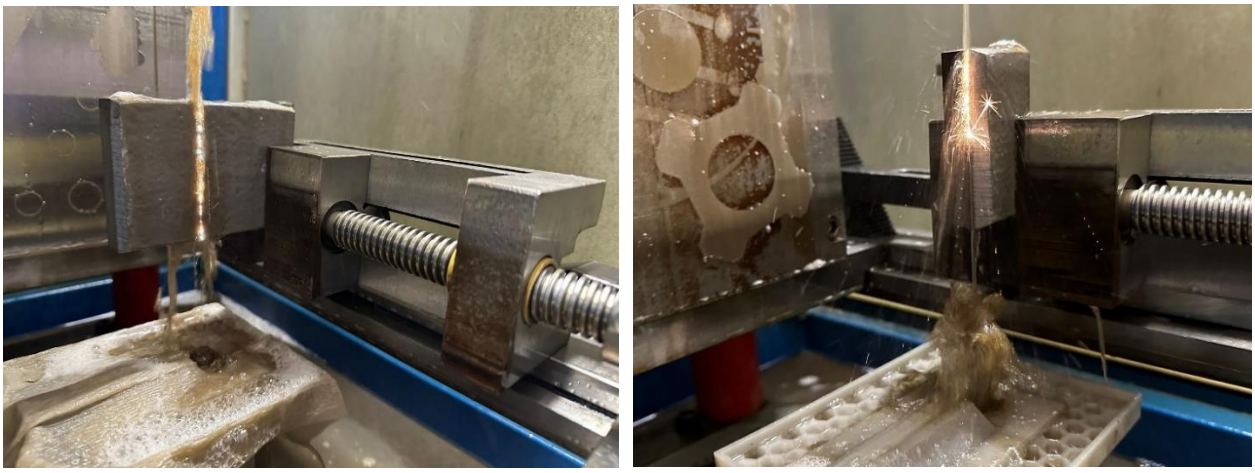

Figure 2-19: Thickness preparation of the A36 steel substrate

Tensile coupons

From there, the final step is obtaining the tensile coupons from the remaining plate. In this case, the steel substrate is placed horizontally to enable direct cutting of all coupons. An AutoCAD program is prepared prior, which helps with designing the cutting of the tensile coupons on the correct dimensions. In Figure 2-20, the final step of cutting and the obtained specimens are shown from the EDM process.

Figure 2-20: Final cutting and tensile coupons obtained with EDM

Any imperfections due to the EDM process are corrected with the polishing process. In the polishing process the tensile coupons are attached to a sticky tape to fasten the grading process. Besides that, different sand grades are selected based on the thickness that needs to be corrected. The final product is a tensile specimen that has similar thickness along the length of the coupon (Figure 2-21). This will prevent any undesired testing effects, such as early failure or lower stiffnesses. Finally, the dimensions of all coupons are noted for prior data analysis. Besides, the Instron uses the thickness and width of the specimen as data for calculating the stress applied to the specimen.

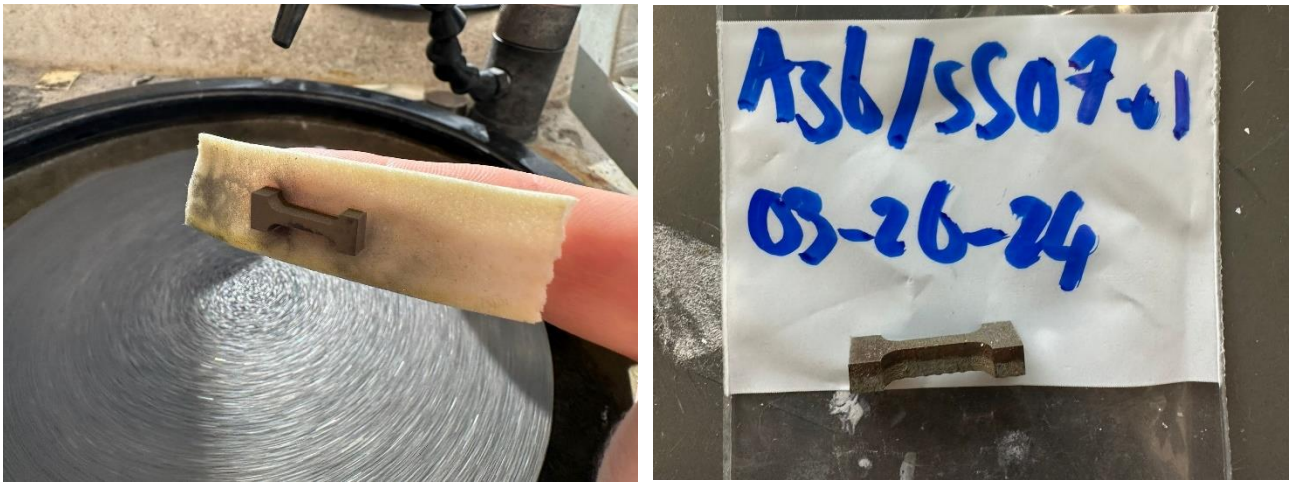

Figure 2-21: Tensile coupon obtained with EDM

Finally, a testing rig is fabricated as holder for the tensile coupons to ensure proper testing. Each specimen is placed and clamped in the holder and taped on the outer side to prevent it from falling (Figure 2-22). Furthermore, an example of a tested coupon is shown on the right in Figure 2-22. Multiple failures and cracks are observed on the cold spray side of the specimen. In the Results section, a deeper discussion of results is given for a better understanding.

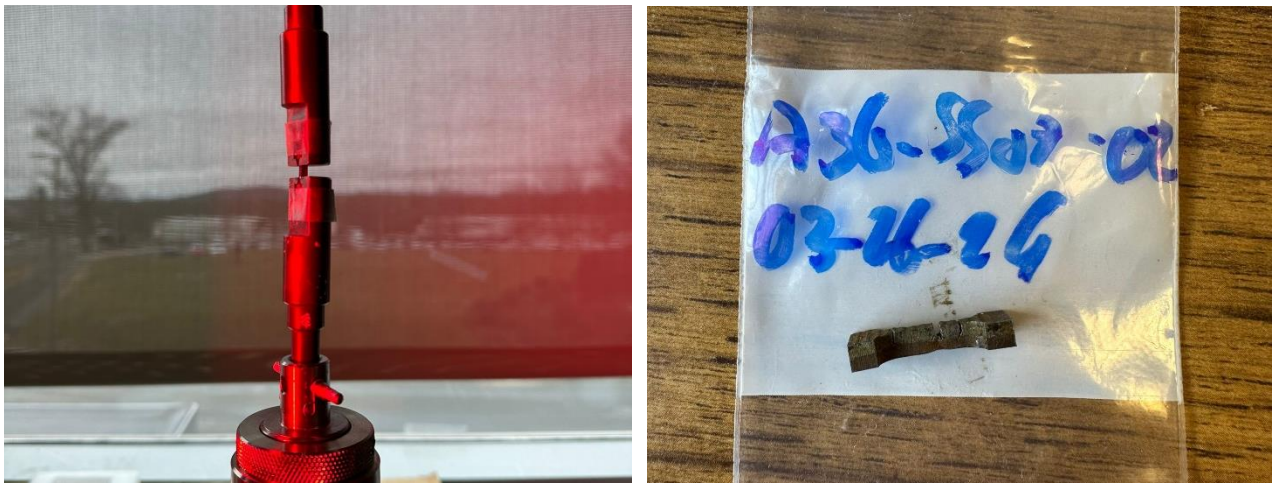

Figure 2-22: Testing rig tension coupons and end result of a composite coupon

Compression pillars

Besides the tension coupons, the compression pillars are prepared for testing. This process is less complicated and requires a simple 2 × 2 × 12 mm strip, which is then cut into three pieces of 2 × 2 × 4 mm. An example of a composite SS08-A36 specimen is shown in Figure 2-23. Due to load constraints, the compression pillars are small to prevent excess loading on the machine. An example of a tested compression pillar specimen is shown on the left in Figure 2-23. Throughout the experiment the specimen shows good bonding. Besides that, it is the brittle behavior of the cold spray part that results in failure of the specimen.

Figure 2-23: Testing rig for compression pillars

This page left blank intentionally.

3.0 Results

From all specimens created through the research methodology described in the previous section, the results are gathered and discussed in this section. The results of steel A36 base material is discussed at first. Furthermore, the repair technologies PAAM and CSAM are discussed. First, the results in compression are shown and discussed, after which the tension coupons follow.

The goal of the section is to have a deep understanding of the contribution of the additive manufacturing technology to the parent A36 steel material. With that, the conclusions on the advantages and disadvantages of the technologies are drawn.

3.1 Base Material A36

First, the base material A36 is discussed in this section, which is later used as reference in further graphs to understand the additional value of the additive manufacturing technology.

Compression
Figure 3-1 shows the stress-strain graph of the tested A36 compression pillars under axial compression using the Instron 5569. A yield stress of 313 ± 12 MPa is obtained after going through the elastic region. In the elastic region, a modulus of 211 ± 13 GPa is obtained, which is typical for A36 steel. From there, the specimen starts to deform plastically and increases load throughout the entire process. In this experiment, no failure is expected and continuation of strain. Therefore, at 10% strain the test is stopped. A good agreement is observed between the specimens and is used as a reference with the cold spray repair powders.

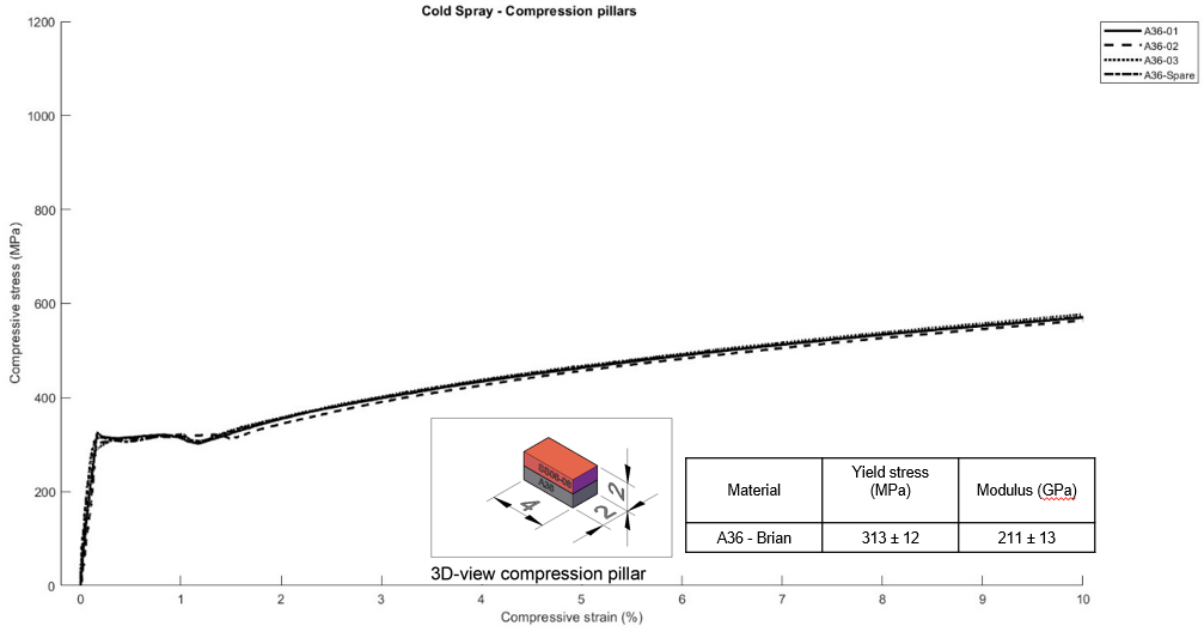

Figure 3-1: Stress-strain curve of A36 compression pillars under uniaxial compression

Tension

Furthermore, Figure 3-2 shows the stress-strain graph of the tested A36 tensile coupons under axial compression using the Instron 5569. A yield stress of 325 ± 12 MPa is obtained after going through the elastic region. In the elastic region, a modulus of 140 ± 4 GPa is obtained, which seems low for A36 steel. It is expected that this comes from the imperfections of the EDM process when cutting, and there are some tolerances here to take into account. In reality, this is not the case for the mechanical properties of A36 being around 200–220 GPa. From there, the specimen starts to deform plastically, starts hardening, and finally necking to failure. This confirms a well-known pattern for the curves as observed for typical A36 steel. Overall, good agreement is observed between the specimens with a large ductility. The tensile material properties are used as comparison with the cold spray repair powders to understand the gain of the repair.

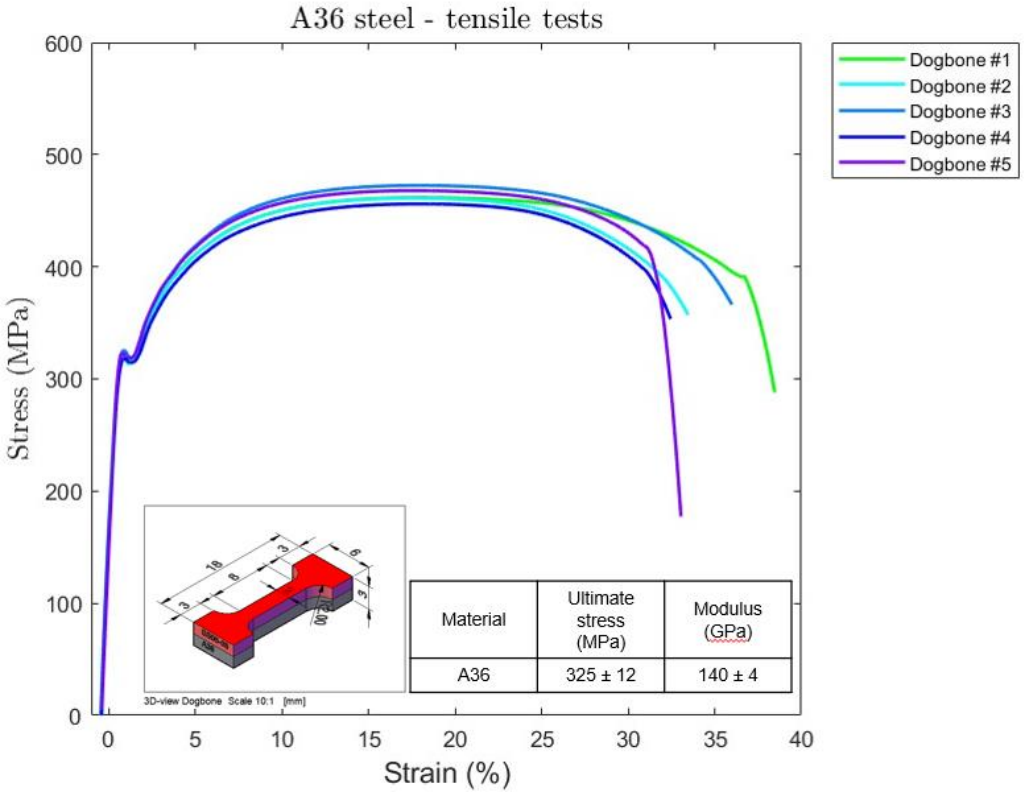

Figure 3-2: Stress-strain curve of A36 tension coupons under uniaxial tension

3.2 Plasma Arc Additive Manufacturing

Results in compression and tension coupons of repair with PAAM are gathered in this section. The chosen print parameters studied in section 2.2 are used to manufacture three specimens for each of the following currents: 125A, 150A and 175A. These three were selected based on the best visible quality of the prints. In Figure 3-3, a stress-strain graph is shown for the results obtained from testing the tensile coupons. As shown, there is no consistency in results, which is fairly problematic. First, inconsistency is observed between the three groups of 125, 150, and 175 A; second, group 125A shows better material properties compared to 150A and 175A. An explanation are the pores that were clearly visible in the specimens, which shows swift failure and large difference in elastic modulus. A last post-processing method of polishing is used to remove most pores throughout, but without large gain in strain.

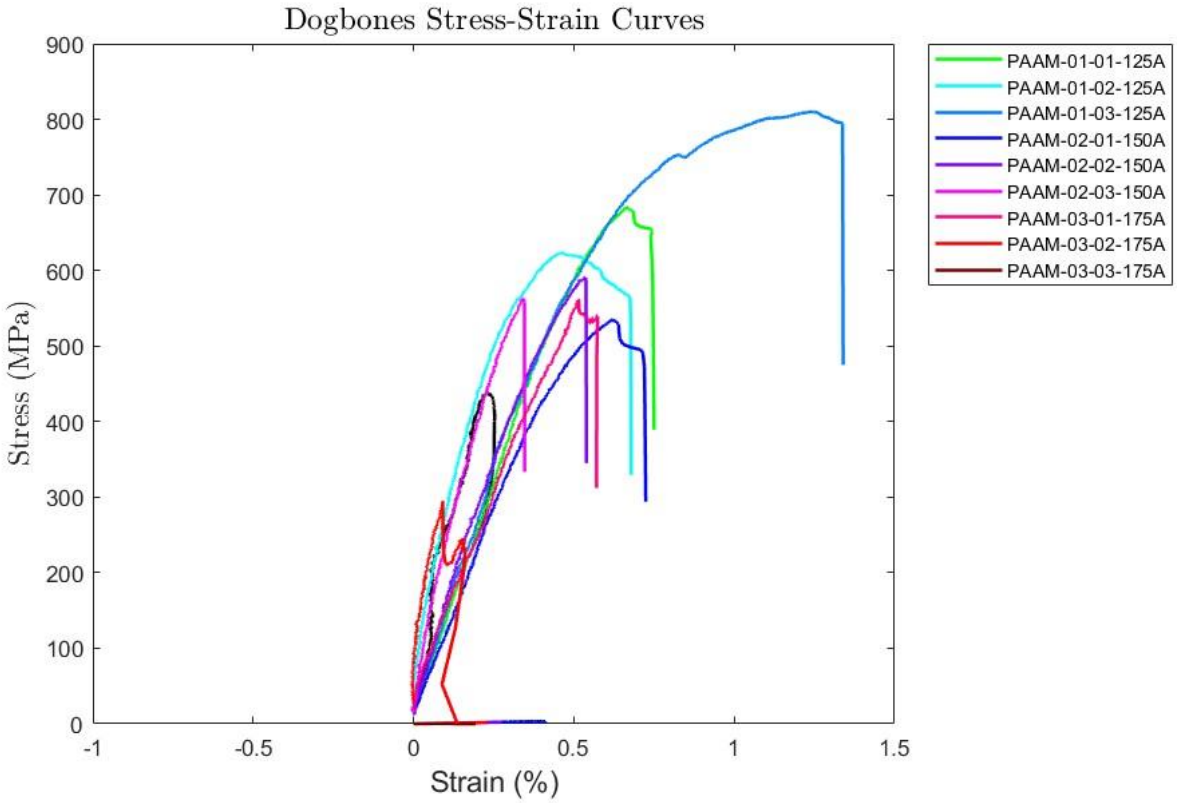

Figure 3-3: Stress-strain curve of PAAM coupons under uniaxial tension

3.3 Cold Spray Additive Manufacturing

Besides PAAM, a similar process is followed for CSAM but extended toward compression, since the repair is generally placed on corroded beam ends, which are almost always under full compression. From here the results are shown and discussed in the following order: WIP-316L, SS06, SS07, and finally SS08.

3.3.1 Powder WIP-316L

Figure 3-4 displays the tensile properties of the A36/316L composites, with yield strength between 140 and 240 MPa, indicative of brittle fracture. In the figure, the stress-strain results are presented of six composite A36/316L tensile coupons, where number 6 is heated for 1 h on 1,000°C. The results show some inconsistency in yield strength between specimens. Overall, a significant strain is obtained that can be explained by the A36 part of the specimen which generally have high ductility characteristics. Cold spray–processed samples usually exhibit premature fracture under tension for various materials due to weak interparticle bonding and a presence of pores discussed in previous studies [47–50].

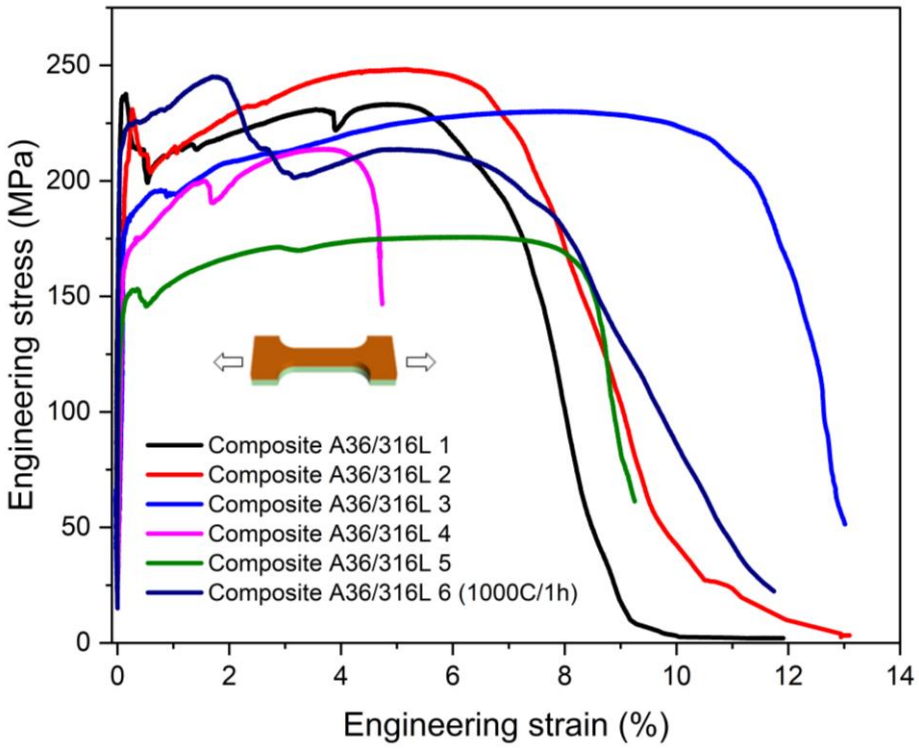

Figure 3-4: Tensile tests of A36/316L composites.

We also examined the compressive performance considering the importance of compressive load within the bridge beam. Figure 3-5 shows the plot of compression tests of pure A36, pure 316L deposition, and A36/316L composites. The compressive yield strength is ~280 MPa for the pure A36 and increased to ~410 MPa in the A36/316L composite, suggesting that the compressive yield strength can be improved far beyond pure A36. In addition, it begins to fail after the strain increases beyond ~5%, suggesting decent plastic deformation under compressive stress. In this figure, in red, the A36 coupons are presented that is the base material, which serves as comparison with the repair material. In black, the result of the compression pillars are presented with high peak stresses and good strains, which show favorable signs to use as repair material against corrosion. Finally, the composite specimens in green show good agreement and great material properties for repair applications.

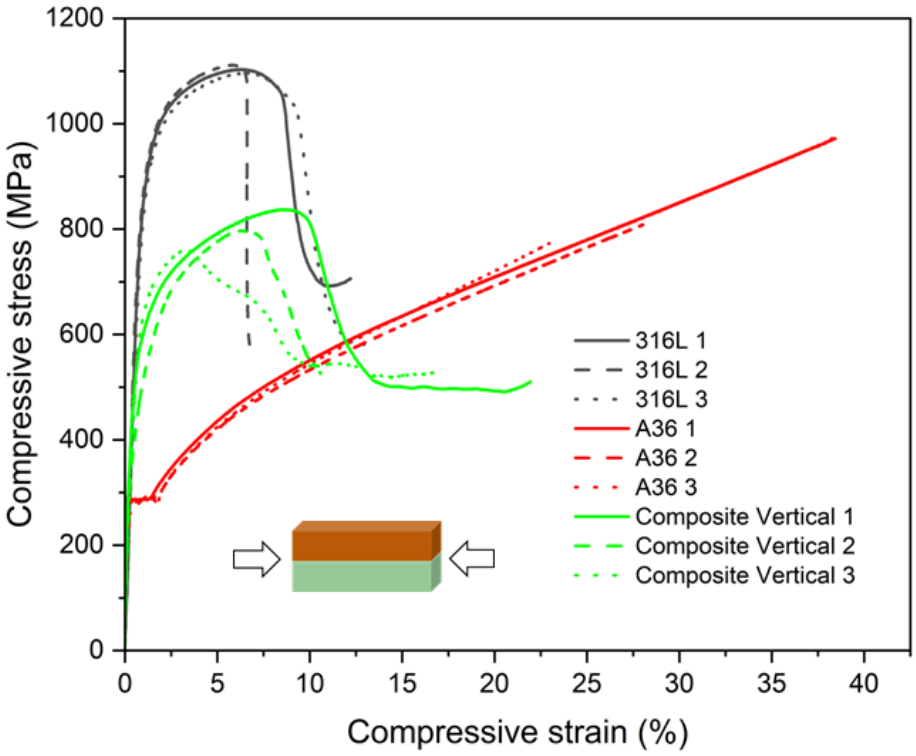

Figure 3-5: Compressive tests of pure A36, pure 316L deposition, and A36/316L composites

Conclusion

In this work, we have performed a systematic study of repairing an A36 steel beam with corroded surface using cold spray by depositing 316L stainless steel powders on the A36 low-carbon steel alloy from degraded steel bridges with WIP-BC1 powder deposited between A36 substrate and 316L deposition. The A36/316L composites exhibit much higher compressive strength than pure A36 low-carbon steel and a compressive strain large than ~5%, which indicates that cold spray can restore the strengths of A36 base metal with decent plastic deformation, although the A36/316L composites exhibit brittle fracture under tension. Our study suggests that cold spray is a promising technique for repairing transportation infrastructure.

3.3.2 Powder SS06

Compression

As discussed previously, the SS06 blend powder is used as a promising candidate for repair. In Figure 3-6 a stress-strain curve for the compression results of pure A36, composite A36/SS06, and pure SS06 is shown. In this figure in black, the A36 coupons are presented for reference purposes compared to the repair material, where pure SS06 in red shows great yield strength characteristics. Besides that, in blue the results for the composite pillars are presented that show good potential as repair application. In comparison with the earlier discussed A36 mechanical properties, the SS06 powder shows promising results in compression. First, the pure SS06 powder shows an astounding 977 ± 50 MPa yield stress. A modulus of 134 ± 1 GPa is obtained, which is significantly lower than conventional

A36 steel. Again, the porosity of the microstructure is a reason for this to drop so significantly. The composite A36/SS06 material shows an expected average of both the pure A36 and SS06. For the composite a 678 ± 22 MPa yield stress and 156 ± 41 GPa elastic modulus is obtained.

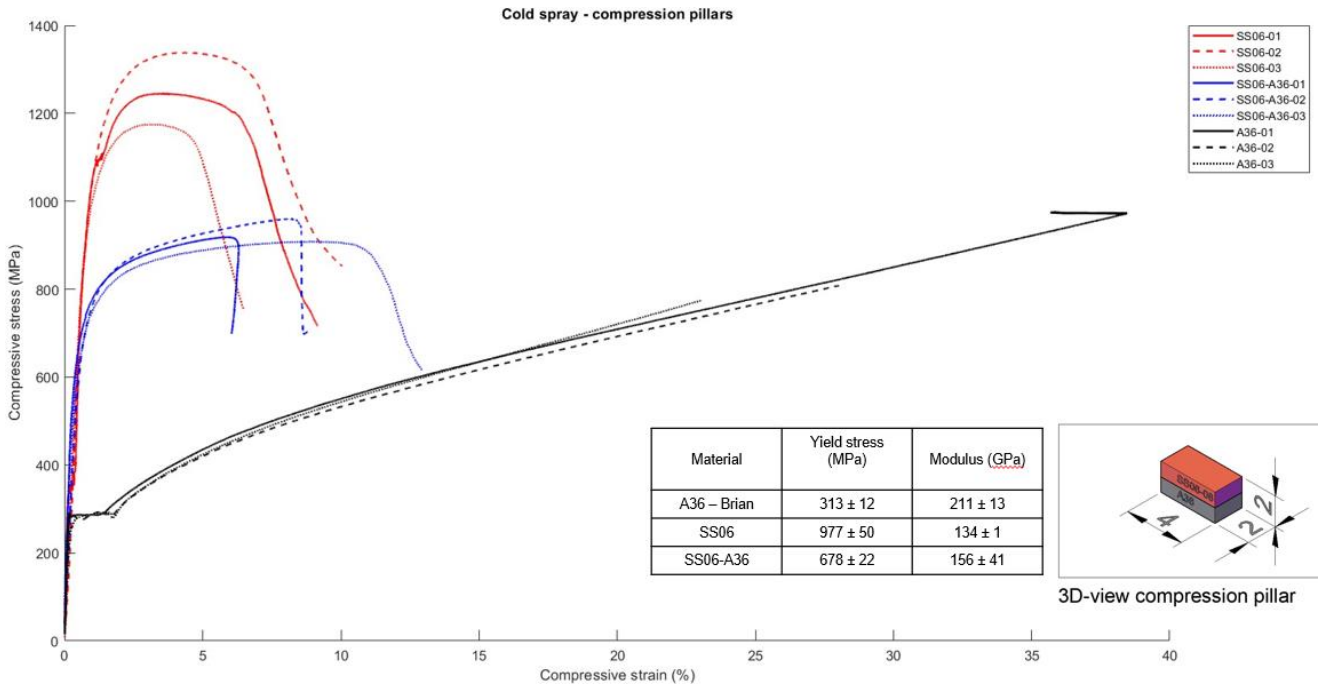

Figure 3-6: Stress-strain curves of pure A36, pure SS06 deposition, and A36/SS06 composites

Tension

In Figure 3-7 a stress-strain graph for the tension results of pure A36, composite A36/SS06 and pure SS06 is shown. In comparison with the earlier discussed A36 mechanical properties, the SS06 powder shows brittle behavior under tension. First, the pure SS06 powder shows a 294 ± 24 MPa ultimate stress. A modulus of 101 ± 1 GPa is obtained, which is significantly lower than conventional A36 steel. Again the porosity of the microstructure is a reason for this to drop so significantly. The composite A36/SS06 material shows a relatively similar behavior to pure SS06, but completely different from A36. For the composite a 318 ± 31 MPa ultimate stress and 134 ± 20 GPa elastic modulus is obtained. Challenges are observed in ductility of the specimens, and repeatability of the composite SS06-A36 specimens is shown to be unfavorable.

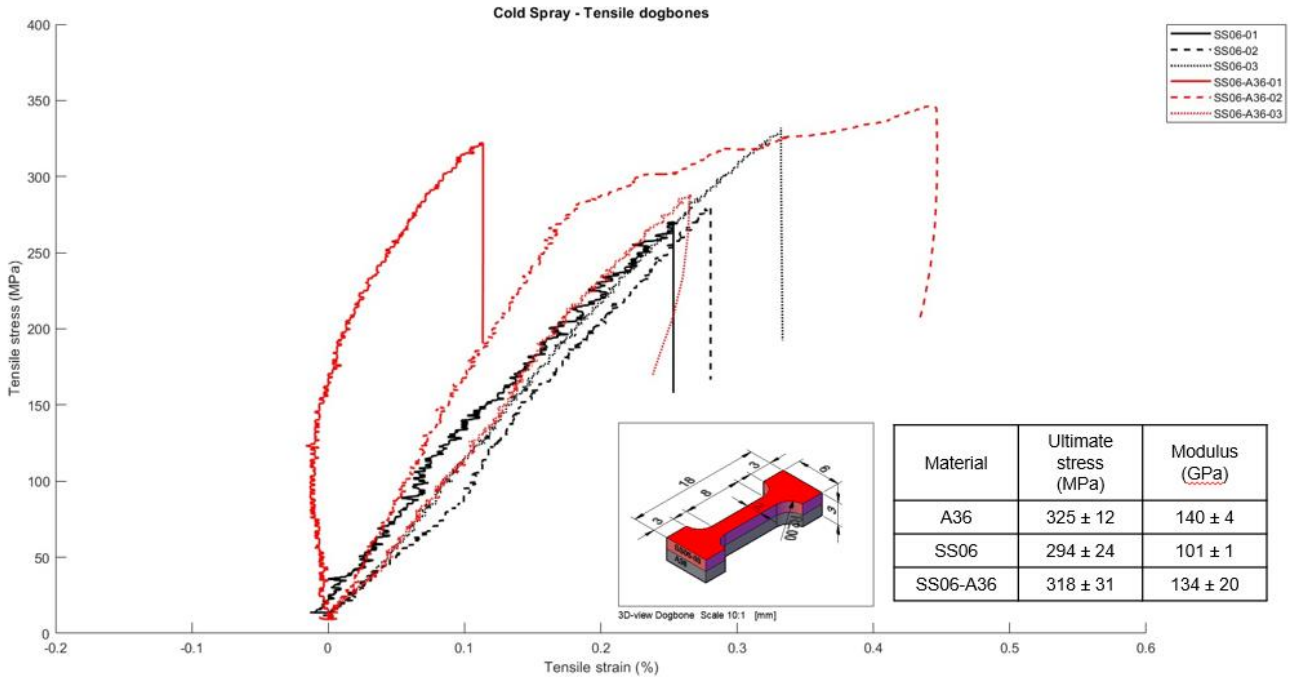

Material	Ultimate stress (MPa)	Modulus (GPa)
A36	325 ± 12	140 ± 4
SS06	294 ± 24	101 ± 1
SS06-A36	318 ± 31	134 ± 20

Figure 3-7: Stress-strain curves of pure A36, pure SS06 deposition, and A36/SS06 composites

3.3.3 Powder SS07

Compression

As discussed previously, the SS07 blend powder is used as a promising candidate for repair. In Figure 3-8 a stress-strain curve for the compression results of pure A36, composite A36/SS07, and pure SS07 is shown. In comparison with the earlier discussed A36 mechanical properties, the SS07 powder shows promising results in compression. First, the pure SS07 powder shows a 681 ± 83 MPa yield stress. A modulus of 262 ± 5 GPa is obtained, which is significantly lower than conventional A36 steel. Again, the porosity of the microstructure is a reason for this to drop so significantly. The composite A36/SS07 material shows an expected average of both the pure A36 and SS07. For the composite a 539 ± 48 MPa yield stress and 235 ± 10 GPa elastic modulus is obtained. Favorable yield stresses and ductility are obtained for the pure SS07 and composite SS07-A36 coupons. Also, SS07 is showing great potential for use as repair to steel corroded elements.

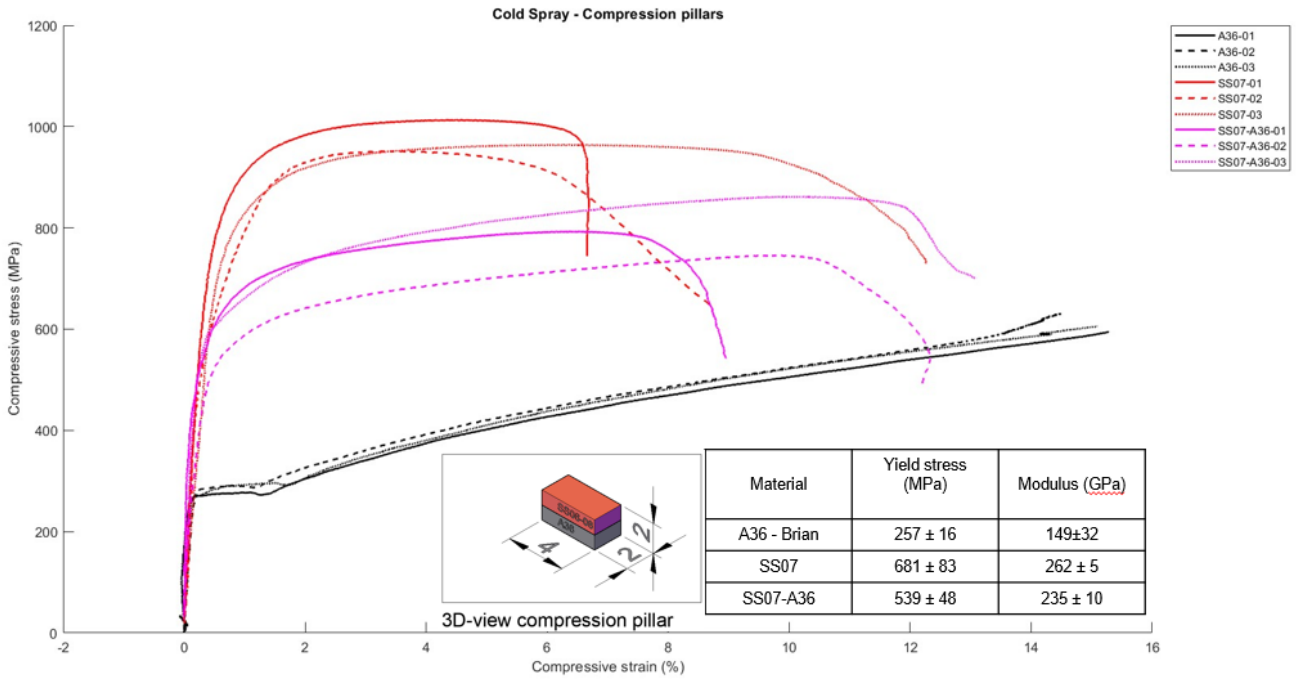

Figure 3-8: Stress-strain curves of pure A36, pure SS07 deposition, and A36/SS07 composites

Tension

In Figure 3-9, a stress-strain graph for the tension results of pure A36 and pure SS07 is shown. In comparison with the earlier discussed A36 mechanical properties, the SS07 powder shows brittle behavior under tension. First, the pure SS07 powder shows a 165 ± 2 MPa ultimate stress. A modulus of 94 ± 3 GPa is obtained, which is significantly lower than conventional A36 steel. The porosity of the microstructure is a reason for this to drop so significantly. Challenges are found in the material properties under tensile loading. Also, an outlier is obtained, which shows the difficult repeatability of the specimens.

In Figure 3-10 a stress-strain graph for the tension results of pure A36 and A36/SS07 is shown. The composite A36/SS07 material shows an relatively similar behavior to pure SS07 but completely different from A36. For the composite, a 245 ± 6 MPa ultimate stress and 272 ± 147 GPa elastic modulus is obtained. The A36 part of the coupons are allowing a significant yield in the specimens. However, specimen 03 and 04 are showing early failure after reaching the yield stress, which shows difficult repeatability.

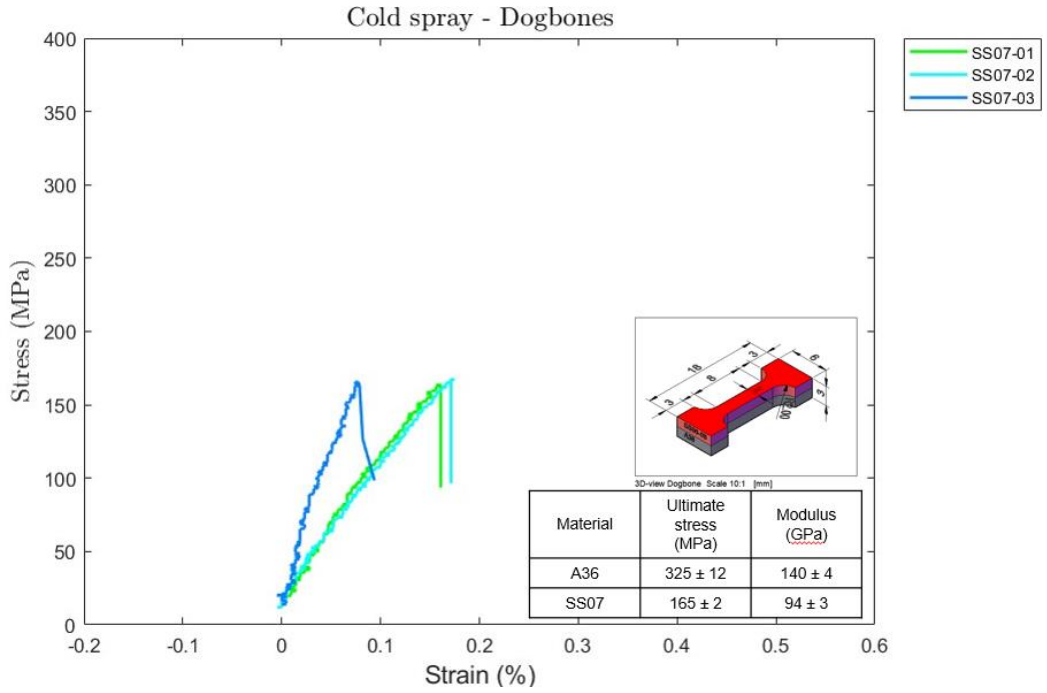

Figure 3-9: Stress-strain curves: pure A36 and pure SS07 deposition tension coupons

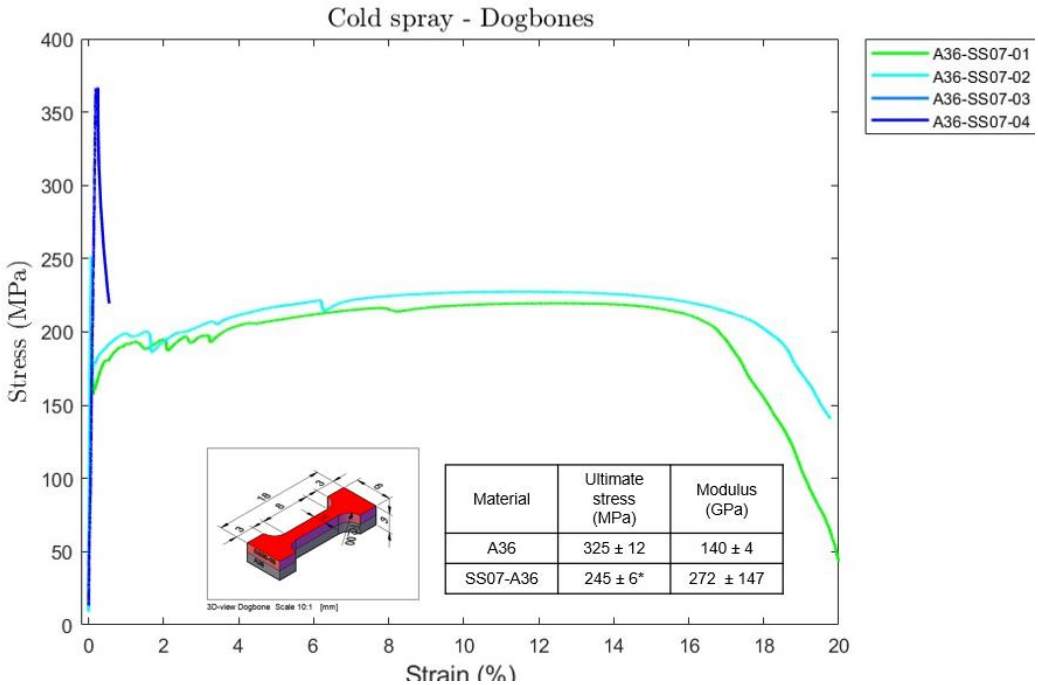

Figure 3-10: Stress-strain curves: pure A36 and composite A36/SS07 deposition tension coupons

3.3.4 Powder SS08

Compression

As discussed previously, the SS08 blend powder is used as a promising candidate for repair. Figure 3-11 shows a stress-strain curve for the compression results of pure A36, composite A36/SS08, and pure SS08. In comparison with the previously discussed A36 mechanical properties, the SS08 powder shows promising results in compression. First, the pure SS08 powder shows a 748 ± 56 MPa yield stress. A modulus of 211 ± 42 GPa is obtained, which is very similar to the conventional A36 steel. The composite A36/SS08 material shows an expected average of both the pure A36 and SS07. For the composite, a 467 ± 40 MPa yield stress and 202 ± 28 GPa elastic modulus is obtained, which is quite promising. Great repeatability is found for the SS08 specimens. The composite curves show great increase in yield and ductility is largely maintained, which shows unique capabilities for use in the field for repair applications.

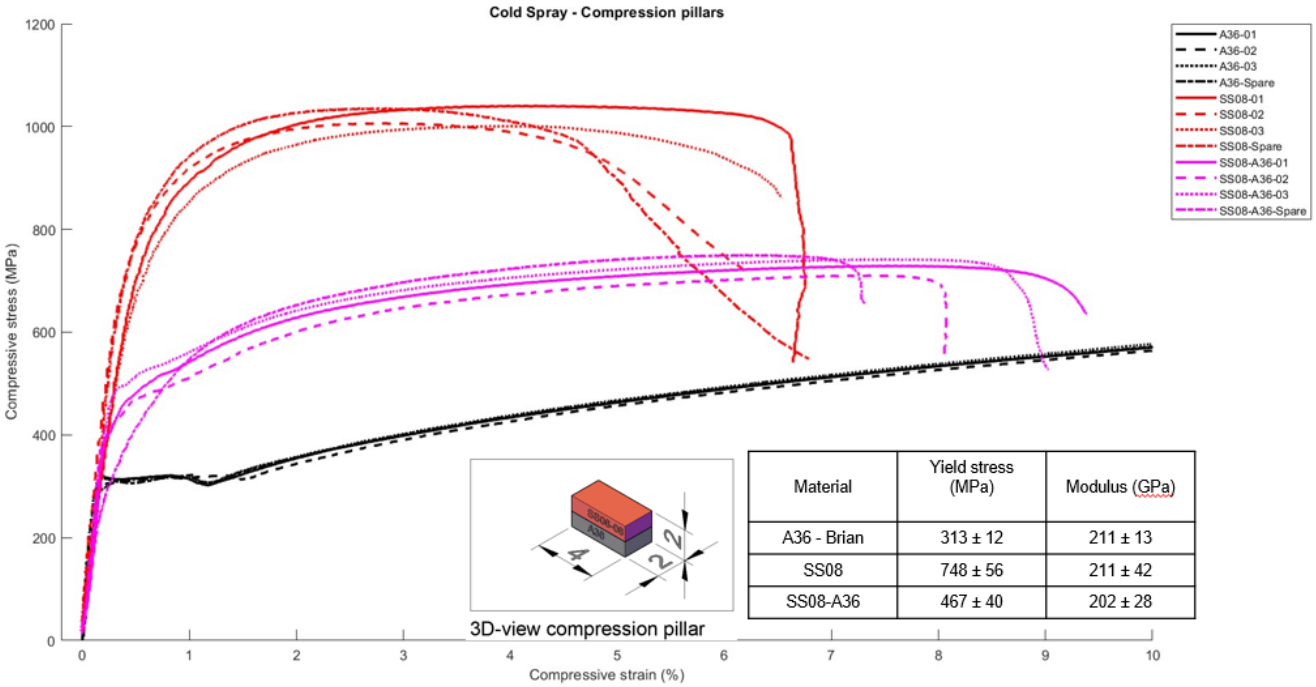

Figure 3-11: Stress-strain curves: pure A36, pure SS08 deposition, and A36/SS08 composites

Tension

Figure 3-12 shows a stress-strain graph for the tension results of pure A36 and pure SS08. In comparison with the previously discussed A36 mechanical properties, the SS08 powder shows brittle behavior under tension. First, the pure SS08 powder shows a 211 ± 18 MPa ultimate stress. A modulus of 163 ± 76 GPa is obtained, which is slightly lower than conventional A36 steel. The porosity of the microstructure is a reason for this to drop so significantly. Challenges are found in material properties here in terms of ultimate strength, repeatability and ductility.

Figure 3-13 shows a stress-strain graph for the tension results of pure A36 and A36/SS08. For the composite, a 243 ± 40 MPa ultimate stress and 226 ± 89 GPa elastic modulus is obtained. Where the

A36 specimens are presented in black and the composite specimens in red. The A36 specimens overall outperform the SS08-A36 specimens.

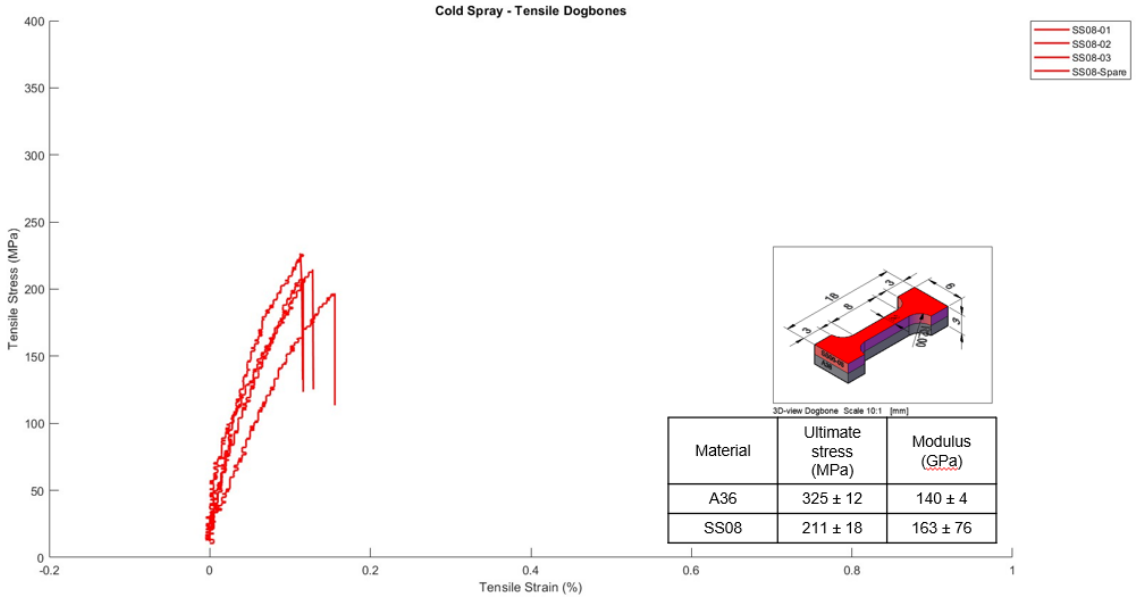

Figure 3-12: Stress-strain curves: pure A36 and pure SS08 deposition

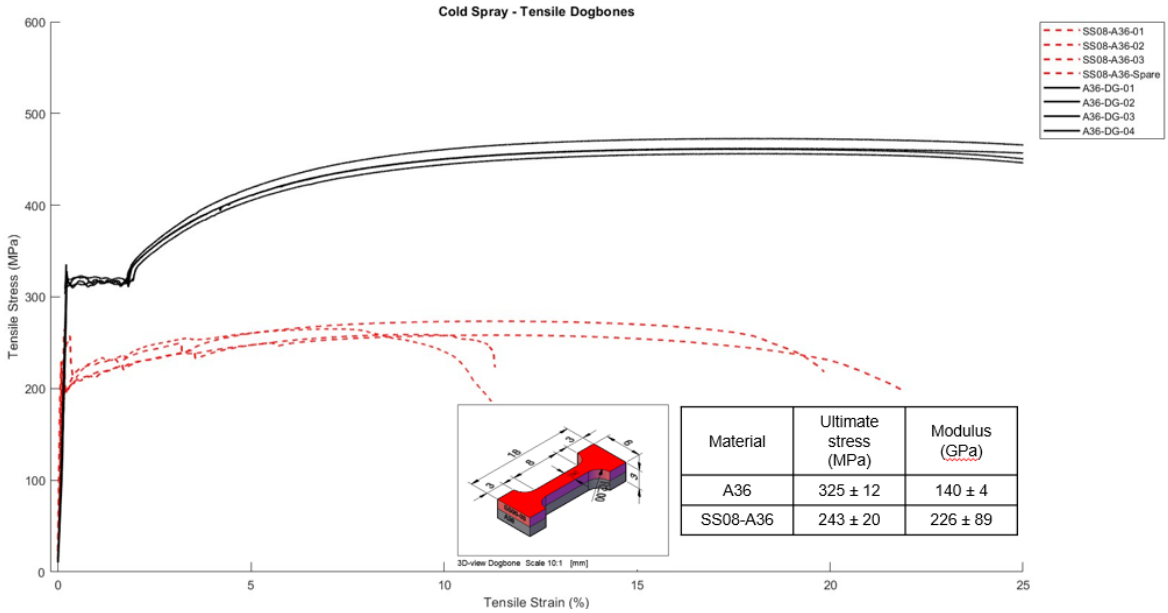

Figure 3-13: Stress-strain curves: pure A36 and composite A36/SS08

3.3.5 Conclusion

In this section, an overview of the results of using CSAM as technology for repair of steel corroded bridge beams is given. The results are divided in compression and tension as shown in Tables 3-1 and 3-2.

Table 3-1: Compression pillar results of various CSAM powders

Material	Yield stress (MPa)	Modulus (GPa)
A36-Brian	313 ± 12	211 ± 13
A36-Shengbiao	280 ± 10	218 ± 20
316L	852 ± 23	110 ± 5
316L-A36	407 ± 44	150 ± 16
SS06	977 ± 50	134 ± 1
SS06-A36	678 ± 22	156 ± 41
SS07	681 ± 83	262 ± 5
SS07-A36	539 ± 48	235 ± 10
SS08	748 ± 56	211 ± 42
SS08-A36	467 ± 40	202 ± 28

Table 3-2: Tensile dogbone results of various CSAM powders

Material	Ultimate stress (MPa)	Modulus (GPa)
A36	325 ± 12	140 ± 4
SS06	294 ± 24	101 ± 1
SS06-A36	318 ± 31	134 ± 20
SS07	165 ± 2	94 ± 3
SS07-A36	245 ± 6*	272 ± 147
SS08	165 ± 2	94 ± 3
SS08-A36	243 ± 20	226 ± 89

This page left blank intentionally.

4.0 Cost Analysis

In addition to the technical feasibility of the cold spray repair method described previously, the study aimed to assess the economic feasibility of cold spray through an activity-based costing (ABC) model. Activity-based costing is a standardized method for calculating the cost of a given manufacturing task (e.g., the production of a fixed quantity of parts). For a typical costing exercise, the total cost is described as the sum costs of a series of individual, discrete, and unique elements. For each of these elements, costs can then be allocated depending on the appropriate scheme.

For example, to calculate the cost of a simple manufacturing process to produce a single unit, the total cost is typically expressed as the sum of the following cost elements: materials, labor, equipment, and overhead (which may contain other elements such as electrical costs or nonproduction workers). Thus, the total cost of a given activity can be expressed as follows:

$$C_t = C_m + C_I + C_{eq} + C_o$$

Where
C_t = Total cost of a manufacturing process,
C_m= Total cost of material,
C_l = Total cost of labor,
C_{eq}= Total cost of equipment, and
C_o = Total cost of overhead.

This method is used widely for cost calculation due to its relatively simple implementation and, when the inputs are modeled at a high level of fidelity, its overall accuracy [62]. Because ABC is most commonly used to model discrete parts manufacturing, there are important additional considerations to mention when applying it to field repair that will be mentioned where relevant.

For the purpose of analyzing the cold spray repair method, we use an ABC model with the same inputs described previously. In the following sections, we will describe the inputs used to model each of the terms in the overall costing function and how those inputs are allocated to different activities. To facilitate the analysis, a static target deposition mass of 1.5 kg is used as a reference. This is an approximation for a relatively minor repair activity.

4.1 Cost of Material

Material costs in cold spray deposition comprise multiple elements. First, there is the primary material that is being deposited onto the substrate. In addition to the primary deposition material, there are other associated consumable costs with the repair, in particular, the cost of gas consumed during the deposition and the cost of electricity associated with the repair. In aggregate, the cost of material is

thus best expressed by the following equation:

$$C_m = C_p + C_g + C_e$$

Where
C_m = Total cost of material,
C_p = Total cost of powder,
C_g = Total cost of gas, and
C_e = Total cost of electricity.

The cost of powder is the total cost of powder that is consumed during the process, which includes both material that is effectively bonded to the substrate during deposition as well as powder that is lost due to poor adhesion. The ratio of bonded to unbonded powder is called the deposition efficiency (DE). Experimentally, we observe a DE of 34% when using the SS08 powder. This is generally lower than typical DEs greater than 50% [63], which could be due to a combination of factors related to the machine configuration (insufficient preheating and/or pressure), or due to the incomparability of the SS08 material to commonly used materials in the literature (e.g., copper and aluminum, which are considerably softer than stainless steel). Additional experimentation is planned to improve the DE.

Powder that is not bonded to the substrate can be reused (once blended with "virgin" powder), although the DE of blended materials will continue to decrease as the recycled powder's morphology is no longer spherical and may be work-hardened during the initial spray activity.

Thus, the cost of powder on a per-spray basis is better expressed as the sum cost of both bonded and lost (i.e., cannot be reclaimed/recycled) powder as well as the cost of the reclamation activity (but not the cost of the powder itself that is reclaimed, as that powder cost is better allocated to a future activity where it is consumed for use).

In total, material cost can be expressed as follows:

$$C_p = \left[\left(M_{pb} + M_{pl}\right) \times C_{pm}\right] + M_{pr} \times C_{pr}$$

Where
C_p = Total cost of powder,
M_{pb} = Mass of powder bonded,
M_{pl} = Mass of powder lost,
C_{pm} = Cost of powder by mass,
C_{pr} = Cost of powder reclamation per mass, and
M_{pr} = Mass of powder to be reclaimed.

The cost of the SS08 material used in the experiments described previously is $40/lb when purchased in 5-lb quantities. Typical costs for stainless steel powders when purchased in larger quantities range from $20 to $40/lb; therefore, bulk purchasing cost is estimated at $30/lb.

The C_{pr} cannot be defined experimentally because there is no mechanism with current equipment to effectively reclaim powder. In addition, it is not assumed that powder reclamation results in perfect yield due to the deformation mechanisms described previously. Additional experimental efforts could define a reclamation efficiency (or RE) that is then used to effectively calculate costs from recycling activity. If RE is known, then calculating M_{pl} and M_{pr} is simplified to the following:

$$M_{pl} = \left(DE * M_{ps}\right) * 1 - RE$$

and

$$M_{pr} = \left(DE * M_{ps}\right) * RE$$

M_{ps} = Mass of sprayed powder, that is, all powder that is sprayed whether or not it is deposited.

Modeling demonstrates the significance of the RE value to the overall costs of material in a given repair. Table 4-1 uses several exemplary values to illustrate the significance of RE to the overall material cost structure of a repair.

Table 4-1: Cost scenarios

Term	Units	Scenario 1	Scenario 2	Scenario 3	Scenario 4
Mass of powder sprayed	kg	2.27	2.27	2.27	1.18
Deposition efficiency	%	34	34	34	65
Target mass	kg	1.5	1.5	1.5	1.5
Cost per mass of powder	$/kg	66	66	66	66
Reclamation efficiency	%	25	50	75	25
Mass of powder lost	kg	1.12	0.75	0.37	0.31
Mass of powder reclaimed	kg	0.37	0.75	1.12	0.10
Total cost of powder	$	125.40	100.32	75.90	71.28
Powder cost attributable to waste	%	59	49	32	10.4

At low RE values (Scenario 1), the cost of powder loss can dominate the cost structure due to the relatively low DE for the SS08 material using our initial experimental settings. When significant powder is lost, low yield during reclamation results in a greater fraction of waste material than deposited material. At high RE values (Scenario 3), although the DE is unchanged, the cost of powder loss is still significant but is reduced considerably and no longer exceeds the cost of deposited material. Importantly, powder waste costs can be reduced when modeling a higher DE similar to those demonstrated in Table 4-1 for other materials (Scenario 4). Despite the low RE value, this scenario is the least expensive scenario modeled due to the decrease in powder required to achieve the same target deposited mass.

In the case of using cold spray deposition on a bridge beam in field, it is difficult to predict the effective RE without further experimentation. On the one hand, means of point-capture of waste (powder loss, rust, paint) is necessary for the cold spray repair method to be suitable for use on bridges in the field, and thus it can be assumed such a capture solution will exist when modeling a mature deployment of cold spray. Those solutions for waste capture would also necessarily capture powder lost during the deposition, which could then be reused. On the other hand, it is impossible to estimate either the reclamation efficiency or the cost of reclamation insofar as both the mechanism for capturing and for processing the waste (i.e., separating reusable powder from waste products) are not yet defined. To be suitable for further use, recycled powder must retain its spherical shape and be free of contaminants (e.g., rust flakes); it is uncertain if either of those conditions are feasible in a field setting. Future work to identify this feasibility and the associated costs of reclamation is necessary to get a holistic view of material cost. For the purposes of this model, we assume that no powder can be reused; thus 100% of powder used (both deposited and lost) during the spray is included in cost.

Moving beyond the cost of powder, we then consider the other consumable costs of gas and electricity. The cost of gas is expressed simply as

$$C_g = \left(C_{gl} * SLM\right) * T_s$$

Where
C_{gl} = Cost of gas per liter,
SLM = Standard liters per minute, that is, nominal consumption per minute in liters, and
T_s = Time during spray.

Ideally, the values for each term in the function are known. Process gas is a commodity that can be quoted by a vendor such as Airgas or Linde. Gas consumption and spray time can be taken directly from in-process monitoring during the deposition process. Figure 4-1 shows the reporting read-out of the VRC software monitoring system that oversees the deposition.

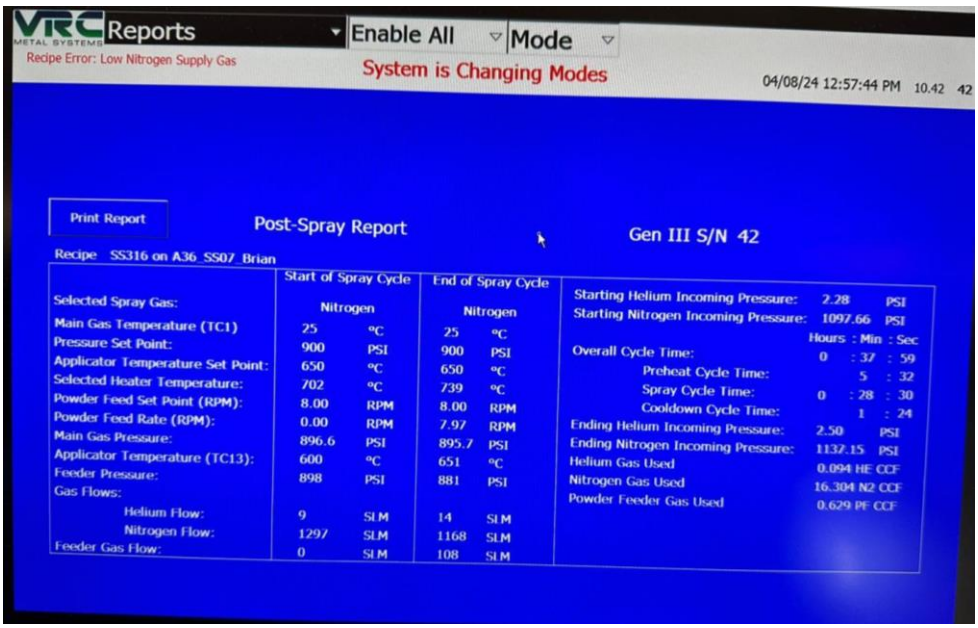

Figure 4-1: Post-spray report using the GEN III system for SS08 powder deposition

This function is also suitable for predicting the cost of gas during a repair when the time during spray can be estimated based on the amount of material intended to be deposited. Using a volumetric constant deposition rate (the amount of powder that is deposited expressed in grams per minute), we can then derive the estimated spray time by dividing the target mass by the estimated deposition rate. The deposition rate can be determined analytically as demonstrated in literature [64]. In this case, the DE is a significant factor on the overall rate of deposition, as a higher yield during deposition significantly reduces the total time (and process gas) required to complete the repair. In a laboratory setting, alternative gas mixtures (e.g., those that use helium as the primary carrier gas instead of nitrogen) can be used to improve deposition efficiency by increasing nozzle pressure and therefore particle velocity. In a field environment high-purity helium is infeasible for both transportation and cost; therefore, this study only considers nitrogen as the primary gas used in the process.

For the present research, we opt to estimate the volumetric deposition rate empirically to avoid the assumptions required for a holistic analytical model. Instead, we measure the time and material volume deposited during a single pass deposition and extrapolate this to a single idealized deposition rate. For a single deposition pass with a given length of 67 mm (~2.6 in.), the time during deposition is approximately 1 sec, with a width of .5 mm and height of .127 mm, which results in a volumetric deposition rate of 4.25 mm^3/sec or 0.255 cm^3/min. This method is limited in its accuracy because it both overestimates and underestimates important parameters. The traverse speed and control of the nozzle in a laboratory setting is controlled and likely much faster than a field repair, especially if the nozzle is hand-held by a human operator. However, the DE for the experimental SS08 material under current settings is impactfully lower than those realized for more commercially demonstrated materials and can likely be improved significantly. To characterize these parameters for a field repair application, further technical demonstrations are required using more appropriate specimens and environmental conditions.

Despite limitations, the volumetric deposition rate is a usable benchmark for estimating process time. Using this value, we can calculate the cost of gas consumption (Table 4-2).

Table 4-2: Gas consumption costs

Term	Units	Value
Target mass of deposit	kg	1.5
Deposition efficiency	%	34
Total mass of material	kg	3.77
Volumetric deposition rate	g/min	.255
Gas consumption rate	SLM	1,200
Cost of nitrogen	$/$m^3$	$1.88*
Estimated spray time	min	65.36
Total gas consumption	m^3	78.432
Total cost of gas	$	147.45

*Assumes wholesale pricing is 33% of laboratory scale price for ultra-high purity nitrogen.

Surprisingly, the cost of gas exceeds the cost of powder in the RE scenarios modeled previously. This further illustrates the importance of the DE on costs. At the low DE observed, the process time is increased because it takes more passes to deposit the same target mass of material. If process time were reduced as a result of an increased DE, gas consumption would also be reduced. This finding is

similar to that demonstrated in another study [65] (Figure 4-2), where gas cost, as a fraction of overall process cost, is greatest when the least efficient combination of machine parameters (and thus the lowest DE) is selected. At higher DE values, gas cost is reduced to ~30% of the overall process cost and ~50% of the cost of powder.

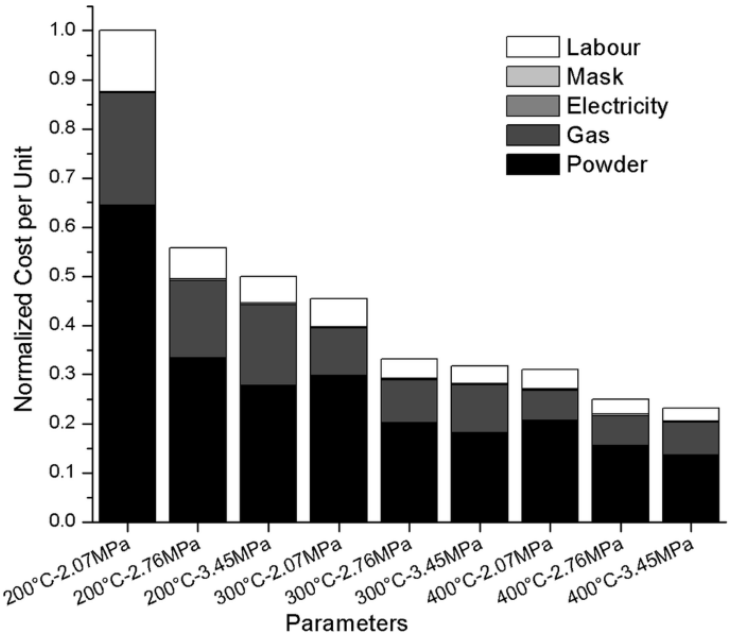

Figure 4-2: Relative cost drivers at different DEs

These costs underestimate the true cost of gas when considering a field setting. Both direct costs (e.g., transportation, loss due to leakage) and indirect costs (e.g., permitting) would increase the cost of gas—and likely substantially due to the large quantity of gas required on site—during a field repair. To avoid these costs, portable systems can use secondary equipment to generate nitrogen on site, but the rate of generation (and the cycle time required to yield full pressure gas necessary for deposition) has not been characterized. These systems will reduce or eliminate the costs of gas transportation, but they may increase overall process cycle time and increase other cost elements of the process.

Last, the cost of electricity required to operate the system and its subcomponents (e.g., the compressor used in field portable equipment) must be considered. In laboratory settings, the cost of electricity is negligible and comprises less than 1% of overall costs. In a field environment, the cost of supplying electricity would be significantly increased due to the requirement to supply fuel to the generator used for the cold spray equipment's operation. It is difficult to analytically estimate these costs without making too many assumptions. Fuel prices are volatile and subject to unpredictable, often global, factors. Electrical load will vary depending on process and environmental conditions; for example, preheating of the powder and nozzle has a significant influence on improving DE, but may take substantially longer when outdoor temperatures are low. Ambient humidity may affect powder flowability, and low temperatures may require longer cycle times due to the need for compressed gas during deposition. Compounding this issue is that limited data exist for the electrical load during operation of the complete system envisioned for field use. Therefore, while we cannot accurately account for these costs until further experimentation is done to characterize the aforementioned factors, it is nonetheless appropriate to say these costs will be significant. For example, a 1 kW diesel

generator operating at half load continuously for an hour consumes approximately 36.4 gallons, equating to $149 using May 2024 average costs of diesel fuel [66]. Considering that several subsystems require power during spray (including the cold spray system itself, the compressor, nitrogen generator, dust collector, and so forth), this is likely a significant underestimate of the total electrical load and associated fuel costs for field operation.

In summary, the consumable costs for field deposition, assuming no improvement in the DE or other process factors, are on the order of $150–$250/kg of deposited material, and perhaps much higher depending on the yet to be defined costs of electrical supply, transportation, and so forth.

4.2 Cost of Labor

Generally, labor cost is simple to characterize by using standard wage rates and expected process cycle times. By assuming a fully burdened (i.e., including both direct cost of salary and indirect costs of employee benefits and so forth) rate for each laborer, and defining the number of laborers required for given process steps with fixed durations, we can quickly estimate the labor costs associated with repair (Table 4-3).

Table 4-3: Labor cost estimate

Term	Units	Value
Average fully burdened salary	$/hr	32.82[a]
Number of laborers	constant	2[b]
Full-time equivalent	%	100
Spray cycle time	min	65
Cost attributable to spray	$	71.11
Setup time	min	180
Breakdown time	min	180
Transportation time	min	120
Total time estimate	min	545
Total labor cost	$	596.23

[a] Average salary is calculated by referencing Bureau of Labor Statistics data [67] for the typical average salaries for "Welders, cutters, solderers and brazers," which is the closest-equivalent job title to that of a system operator for a manual cold spray system. While the mean national hourly wage for all categories is $25.31 as of most recent data, Massachusetts generally is in the highest wage bracket and has an approximately 23% premium over national averages. In addition, contractors working in the "Foundation, structure, and building exterior" industries, which most closely approximates bridge repair, have a 5% wage premium over the hourly mean wage.

[b] Two operators are assumed both for safety and based on a reasonable expectation of effort required to set up and pack the system before and after a repair activity.

To accurately model labor costs, one must make many assumptions regarding the duration of non-spray activities including travel time to-and-from the repair site, the time required to set up the system (including preheating and gas pressurization), and the time required to pack the system before transporting it back to a central warehouse. These times will be heavily site-dependent given variable conditions in road access, beam elevation, presence of bodies of water, ground environmental conditions, temperature, humidity, and other factors. For the purposes of modeling, fairly

conservative estimates of 3 hours are made for both the setup and breakdown times required. Transportation is assumed as 1 hour from warehouse to site, or 2 hours in total.

The amount of time dedicated to spray is less than the time dedicated to non-spray activities, and therefore the labor costs associated with spraying material are only a small fraction of the total labor cost. This intuitive finding suggests that repair activities that require a larger volume of deposited material (and therefore more time spent spraying) will be more labor cost efficient, because the duration of non-spray activities will be largely fixed (and thus their relative share of total labor cost decreases as spray time increases). This is an imperfect assumption since repair activities taking place on the two extremes of a given beam may require additional setup time. In addition, these cycle times may be increased should multimaterial approaches be desired (e.g., for applying a protective coating or using the spray system to facilitate paint removal via an abrasive medium).

Evaluating the true cost associated with non-spray activities will require further field evaluation to understand the relationship between the aforementioned variable factors in site conditions and the cycle times associated with non-spray activities in the field. For the sake of having comparable results, this report will only carry forward the cost of spray deposition, $71.11, identified previously.

4.3 Cost of Equipment and Overhead

The final two terms in our modeling exercise correspond to the fractional cost of equipment as well as ancillary costs aggregated into a single overhead term. Equipment costs are determined by taking the annualized value of the equipment (i.e., the fractional purchase cost divided by a fixed number of years according to a determined amortization schedule) and multiplying that by the expected time the equipment is occupied. A straight-line depreciation model with a fixed term for all capital equipment is assumed. Other costs (e.g., the interest paid due a creditor if a loan is used to purchase equipment) are not considered but are relevant in scenarios where applicable. Because the VRC Raptor system under PO with UMass Amherst is grant funded, those costs are not relevant to our modeling.

Equipment cannot realistically be used fully (for each hour of each day) during a calendar year. It is more appropriate to understand the annual cost of equipment where the annual term is a set number of hours based on an organization’s working hours and the equipment’s uptime (i.e., when the equipment can be used rather than when it is being serviced).

This assumes the system is nondedicated and the equipment cost for a given repair is only associated with the use of the equipment during the repair activity (and, in this case, limited further only to spraying material). In other words, it assumes that for all periods of time outside of the scope of the modeled repair, the machine is being used and those other uses are bearing their own share of the annual machine cost. This is not necessarily a realistic assumption, as the amount of repair work (and the amount of machine time used) likely cannot scale to match the total availability of the machine system modeled here. Take an extreme example: If only a single repair activity takes place in a calendar year, then the cost of equipment for that single repair would be $53,571. To enable further modeling, we will continue to assume that the machine is nondedicated as described previously and note here that this results in a likely underestimate of equipment costs. Table 4-4 illustrates the cost of equipment on an annual and per-hour basis.

Table 4-4: Equipment and overhead costs

Term	Units	Value
Up-front capital expense	$	375,000*
Amortization period	years	7
Annual cost per year	$	53,571
Available hours per day	hrs	16
Available days per week	days	7
Uptime	%	70
Total available hours	hrs	4,076
System cost per hour	$/hr	13.14
Spray time	hrs	1.01
Total equipment cost attributable to spray	$	14.31
Total machine time	hrs	9.08
Total equipment cost	$	119.31

* The system cost for the exemplary VRC Raptor system, including installation costs and warranties, is approximately $265,000. In addition to the cold spray system itself, a compressor and electrical generator are required for field operation. This equipment must be loaded onto a towed trailer and towed to-and-from the repair site by a work vehicle. The aggregate costs for these additional elements are assumed to be $110,000.

Finally, we consider overhead costs. Overhead is highly dependent on a variety of factors, most importantly the financial structure, payroll, facilities, and other factors related to the organization performing the repair. It is most typical to assign overhead as a percentage of the sum total of other modeled costs. This term cannot be estimated exactly, but several comments can be made for consideration. The cost of overhead associated with facility expenditures is likely substantially less than in a factory-style setting as the equipment is primarily stored and serviced within the facility but is otherwise nonoperational. Costs associated with, for example, house gas supply or electrical consumption would not be nearly as significant when compared to fixed operation of a system within a given facility. These costs are not eliminated but are simply moved to other cost categories as mentioned previously. Due to the comparatively long “sales cycle” for repair activities, and the requirement to invest labor hours in nonrevenue generating activities (e.g., bid preparation, permitting, etc.), staff overhead may be increased relative to other industries that use ABC process modeling. For the purposes of this modeling exercise, a conservative overhead rate of 70% is assumed.

There are both direct and indirect costs associated with the field application of cold spray that are not directly modeled in the preceding analysis. However, for any repair activity, a holistic review of cost drivers is important, and we must consider these factors to some extent. These cost factors relate predominantly to two areas: (1) direct operational costs incurred during the field-spray activity that are not associated with the process of material deposition itself (e.g., the cost of cranes or other lifting devices used to transport the system operator close to the bridge beam), and (b) indirect costs associated with an overall repair activity (e.g., roadway closure or police detail). Our relatively conservative estimation approach considers these costs robustly insofar as it is difficult to accurately predict their costs without field experimentation. A high-level review of additional direct and indirect costs is provided in Table 4-5.

Table 4-5: Additional process costs

Term	Note
Direct Costs	
Cranes and other lifting devices	A single operator can complete the field repair, though a second device may be necessary to hoist the equipment.
Waste storage and disposal	We assume waste can be captured into a single stream via a point-capture device, and waste disposal of nonreactive metals is generally inexpensive
Environmental abatement	We assume waste can be captured at the point of deposition, such that additional environmental abatement is not necessary in typical repair cases. This assumption is integral to the feasibility of CSAM as a repair method, as abatement of highly distributed metal powders on either land or in a water body would be challenging.
Surface preparation	CSAM equipment can be modified to serve as "grit/sand blast" equipment, and thus surface preparation can be modeled according to the same cost structure as the deposition itself. Because the same equipment and waste capture strategy would be used, surface preparation is likely about 5%–15% of the cost of a deposition and affected predominantly by the surface area (and therefore spray time).
Testing and monitoring	We do not propose a specific monitoring method and therefore cannot estimate the cost of monitoring tasks.
Indirect Costs	
Roadway closures	The CSAM deposition method is efficient such that multiple kilograms of structural steel can be deposited within a single day. While the cost of a roadway closure is likely to be unchanged per unit time (i.e., it is expected that it costs the same to close a traffic lane for a single day regardless of why it is being closed), we expect the CSAM method could result in considerably fewer work days and therefore a considerably abbreviated closure period for the roadway above the bridge.

4.4 Total Cost of Spray

Using the function for total cost defined at the beginning of this section, we can then estimate the total cost for the repair modeled as well as estimate the approximate cost per kilogram of deposited material (Table 4-6).

Table 4-6: Total costs for the CSAM process

Term	Units	Value
Powder consumed	kg	2.27
Target mass of deposit	kg	1.5
Spray time	min	65.36
Cost of powder	$	149.82
Cost of gas	$	147.45
Cost of fuel	$	415*
Cost of labor	$	71.11
Cost of equipment	$	14.31
Total direct costs	$	797.69
Cost of overhead	$	558.38
Total cost	$	1,326.01
Cost per mass	$/kg	884

* Given the importance of fuel costs to overall costs, an estimate of 100 gallons of diesel fuel, priced at $4.15 per gallon as of May 2024, are assumed to be used during the spray operation.

Critically, we must stress that these values both significantly underestimate and significantly overestimate costs in certain aspects. The costs are limited only to the costs that can be directly attributable to the cold spray activity (with the exception of overhead). Transportation, permitting, and other costs are not modeled, and the overhead value selected may or may not be sufficient to fully capture those costs. However, the amount of powder and gas consumed is a direct function of DE, and it is a strong possibility that DE can be improved over our initial experimental findings. As demonstrated previously, the DE is the single most important term in determining the cost of spray deposition. To more accurately model the cost of cold spray repair, it is necessary that further variables are empirically characterized in a field (or field analogous) setting.

This page left blank intentionally.

5.0 Implementation and Technology Transfer

In this section, a description is given on how the work presented in this report is used for future implementation and research work. The expansion of the work will be twofold: further extension of testing toward bending and fatigue testing, and moving from the lab environment toward field work. It is a big step forward in the aim to start repairing steel bridges in the field.

5.1 Presented Report

The first way to share knowledge and educate about the potential of additive manufacturing techniques for repair of steel corroded bridge beams is this report. Furthermore, several CSAM applications of powders are discussed and presented using literature and several performed compression and tensile tests. Also, PAAM is studied, a parameter study is performed, and the best performing print parameters were selected. From there, several single tracks of PAAM were applied and tested to obtain the mechanical properties.

5.2 Conference Proceedings

Throughout the year many interesting conferences are given. For this year, we have identified the MassDOT innovation conference, EMI2024, NBPC2024, and the TRB2024 as suitable venues to present the research work on structural repair of steel corroded beam ends using additive manufacturing technologies. A presentation is given in a technical session filled with several key industry academics from the field. With that, ideas and possibilities of structural repair using AM technologies are shared and discussed. Each session ends with some time allocated for questions in which the audience can show their interest and participation. Furthermore, abstracts have been submitted to the two latter conferences with the same goal to educate and share the knowledge [68–71].

5.3 Webinars

Some of the options to educate workers in practice is by holding webinars. During a webinar, a talk is performed on the research to explain and discuss the research work. In the past, many webinars have been conducted for many people from the field of MassDOT. A screenshot of a previous webinar is given in Figure 5-1.

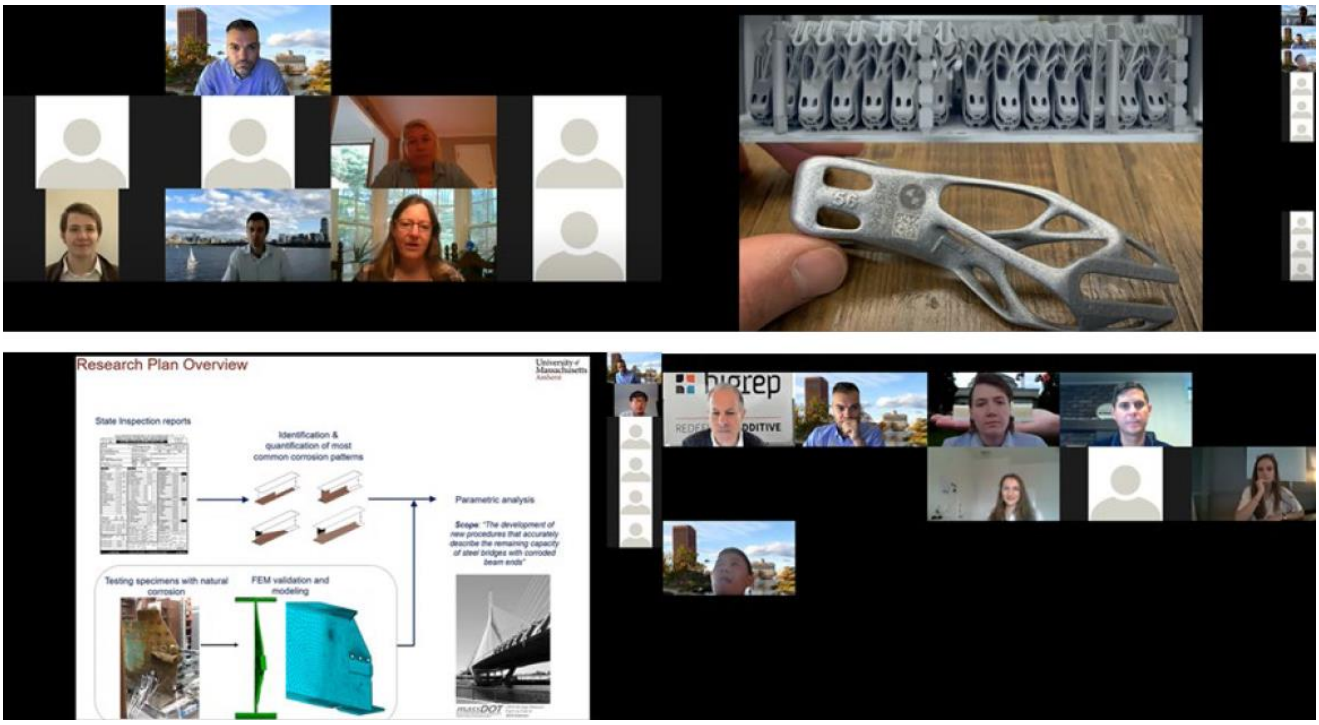

Figure 5-1: Screenshots of previous webinars

5.4 Lab Tours MassDOT, MIT, and UMass Amherst

UMass Amherst tour

During the collaboration between MassDOT, MIT, and UMass Amherst, several lab tours have been organized. At the start of the lab tour an overview presentation is given considering all technologies that research is performed on within this project. A walkthrough of results so far and application possibilities were presented to the MassDOT attendees. The following parts were presented: 3D scanning for bridge inspection, Cold spray additive manufacturing, and cold spray repair of corroded steel beam ends. With that, an idea is given of an entire work process that is worth implementing in the future.

The tour of UMass Amherst and the Advanced Digital Design and Fabrication (ADDFab) lab included selective laser melting (SLM) printers for 3D printing of steel, selective laser sintering (SLS) printers for Nylon prints, and the EDM machine. Furthermore, the PAAM lab is shown where the specimens were presented regarding the parameter studies. Finally, the tour went to the CSAM lab, which is one of the main facilities that is being used for this research project. Again, the specimens and work process of cold spray were discussed to the MassDOT attendees. An impression of the visit is given in Figure 5-2.

Figure 5-2: CSAM lab tour

Finally, the tour ended in the structural engineering Brack lab. With that, a walkthrough of the LiDAR scanning process is presented. In this case, a steel beam is scanned and the results of the scan was directly presented on the screen to have it visible for the audience. With that, the speed of LiDAR scanning is presented, and the 3D model containing thousands of data points is illustrated.

MIT tour

Besides the UMass tour, a MIT tour is organized consisting of a lab tour and presentation. The presentation walked through additive manufacturing in general and how AM has evolved over years. Processes such as 3D printing, polymer extrusion, injection molding, and powder bed fusion were all part of this discussion. From there, the attendees were shown around the mechanical engineering lab, nano lab, and many more to see the machines from the slides in real life.

This page left blank intentionally.

6.0 Conclusions

Several conclusions can be drawn from the research work presented here regarding new potential additive manufacturing technologies.

First of all, PAAM is a technology that has received an increase in attention throughout the industry. From there, the interest of applying PAAM for repair of steel corroded elements is worth considering. The following conclusions are drawn within this research report:

- The single tracks made on the corroded substrate show many visual pore defects throughout, resulting in early failure. Even though a print parameter study was performed, the tracks did not seem to meet the quality needed.
- Even though similar print properties are used, repeatability of the tracks is difficult. As a result, very different results in mechanical properties are obtained.

For CSAM, several compression pillars and tensile dog bones are tested with several powders such as WIP316L, SS06, SS07, and SS08. In this case, tests were performed of pure A36, pure cold spray powder, and the composite A36 cold spray blend, and these are discussed. The following conclusions are drawn:

- Great potential is observed from the results of the compression pillars. The powder has proven to be a big contribution in terms of mechanical properties to the corroded A36 material. Compared to the yield stress of A36 being 313 ± 12 MPa, the SS06, SS07, and SS08 powders obtained 977 ± 50 MPa, 681 ± 83 MPa, and 748 ± 56 MPa of yield stress in that order. However, the contribution of the composite materials is of the main interest being for A36-WIP316L, A36-SS06, A36-SS07, and A36-SS08: ~410 MPa, 678 ± 22 MPa, 539 ± 48 MPa, and 467 ± 40 MPa compared to 313 ± 12 MPa of pure A36.
- The results for the tensile dogbones seem to need more research and development to increase mechanical properties. Strains for the pure powders reached from 0.1% to 0.4% here. This explains a brittle behavior for the powder. Furthermore, the composite specimens A36-WIP316L, A36-SS07, and A36-SS08 showed ductile behavior that is explained by the A36 side of the specimen taking over after failure of the repair.

This page left blank intentionally.

7.0 References

1. ASCE, Infrastructure report card, (2017). https://www.infrastructurereportcard.org/ (Accessed 27 January 2020).
2. FHWA, National bridge inventory database, (2017). https://www.fhwa.dot.gov/bridge/nbi/no10/defbr17.cfm (Accessed 27 January 2020).
3. Z. Guo, Y. Ma, L. Wang, X. Zhang, J. Zhang, C. Hutchinson, I.E. Harik, Crack propagation-based fatigue life prediction of corroded RC beams considering bond degradation, J. Bridge Eng. 25 (8) (2020), https://doi.org/10.1061/(ASCE) BE.1943-5592.0001592.
4. Y. Ma, Z. Guo, L. Wang, J. Zhang, Probabilistic life prediction for reinforced concrete structures subjected to seasonal corrosion-fatigue damage, J. Struct. Eng. 146 (7) (2020), https://doi.org/10.1061/(ASCE)ST.1943-541X.0002666.
5. Y. Ma, Z. Guo, L. Wang, J. Zhang, Experimental investigation of corrosion effect on bond behavior between reinforcing bar and concrete, Construct. Build. Mater. 152 (2017) 240–279, https://doi.org/10.1016/j.conbuildmat.2017.06.169.
6. J.M. Kulicki, Z. Prucz, D.F. Sorgenfrei, D.R. Mertz, W.T. Young, Guidelines for evaluating corrosion effects in existing steel bridges, (1990).
7. T. Roberts, Slender plate girders subjected to edge loading, Proc. Inst. Civ. Eng. 71 (2) (1981) 805–819.
8. J.R. Kayser, A.S. Nowak, Capacity loss due to corrosion in steel-girder bridges, J. Struct. Eng. 115 (6) (1989) 1525–1537, https://doi.org/10.1061/(ASCE)0733-9445(1989)115:6(1525).
9. J.W. van de Lindt, M. Ahlborn Theresa, Development of steel beam end deterioration guidelines, Tech. rep., MDOT Res. Rep. RC 1454 (2005).
10. I. Sugimoto, Y. Kobayashi, A. Ichikawa, Durability evaluation based on buckling characteristics of corroded steel deck girders, Quart. Rep. RTRI 47 (3) (2006) 150–155.
11. I.-T. Kim, M.-J. Lee, J.-H. Ahn, S. Kainuma, Experimental evaluation of shear buckling behaviors and strength of locally corroded web, J. Constr. Steel Res. 83 (2013) 75–89, https://doi.org/10.1016/j.jcsr.2012.12.015.
12. J.-H. Ahn, J.-H. Cheung, W.-H. Lee, H. Oh, I.-T. Kim, Shear buckling experiments of web panel with pitting and through-thickness corrosion damage, J. Constr. Steel Res. 115 (2015) 290–302, https://doi.org/10.1016/j.jcsr.2015.08.032.
13. N. Khurram, E. Sasaki, H. Katsuchi, H. Yamada, Experimental and numerical evaluation of bearing capacity of steel plate girder affected by end panel corrosion, Int. J. Steel Struct. 14 (3) (2014) 659–676, https://doi.org/10.1007/s13296-015-3018-0.
14. J.-H. Ahn, S. Kainuma, F. Yasuo, I. Takehiro, Repair method and residual bearing strength evaluation of a locally corroded plate girder at support, Eng. Fail. Anal. 33 (2013) 398–418, https://doi.org/10.1016/j.engfailanal.2013.06.015.
15. T. Miyashita, M. Nagai, D. Wakabayashi, Y. Hidekuma, A. Kobayashi, Y. Okuyama, N. Koide, W. Horimoto, Repair method for corroded steel girder ends using CFRP sheet. IABSE-JSCE Joint Conference on Advances in Bridge Engineering-III, 2015, pp. 21–22.
16. H. Ogami, K. Fujii, T. Yamada, H. I. Washaki, Renovation of corroded girder end in plate girder bridge with resin and rebars, implementing innovative ideas, Structural Engineering and Project Management, 2015, pp. 1–6.
17. B. Wu, J.-L. Cao, L. Kang, Influence of local corrosion on behavior of steel I-beams subjected to end patch loading: Experiments, J. Constr. Steel Res. 135 (2017) 150–161, https://doi.org/10.1016/j.jcsr.2017.04.020.

18. B. Wu, J.-L. Cao, L. Kang, End patch loading behavior and strengthening of locally corroded steel I-beams, J. Constr. Steel Res. 148 (2018) 371–382, https://doi.org/ 10.1016/j.jcsr.2018.05.029.
19. G. Tzortzinis, B. Knickle, S. Gerasimidis, A. Bardow, S. Brena, Experiments and computations on steel bridge corroded beam ends, in: Proceedings of the Annual Stability Conference, Structural Stability Research Council, St. Louis, Missouri, 2019
20. G. Tzortzinis, B. T. Knickle, A. Bardow, S. F. Breña, S. Gerasimidis, Strength evaluation of deteriorated girder ends. I: Experimental study on naturally corroded I-beams, Thin–Walled Structures 159 (2021) 107220, https://doi.org/10.1016/j.tws.2020.107220.
21. G. Tzortzinis, B. T. Knickle, A. Bardow, S. F. Breña, S. Gerasimidis, Strength evaluation of deteriorated girder ends. II: Numerical study on corroded I-beams, Thin–Walled Structures 159 (2021) 107216, https://doi.org/10.1016/j.tws.2020.107216.
22. G. Tzortzinis, S. F. Breña, S. Gerasimidis, Improved Load Rating Procedures for Deteriorated Steel Beam Ends with Deteriorated Stiffeners, MassDOT report No. 21-024, (2021).
23. G. Tzortzinis, S. F. Breña, S. Gerasimidis, Experimental testing, computational analysis and analytical formulation for the remaining capacity assessment of bridge plate girders with naturally corroded ends, Engineering Structures, 252 (2022) 113488.
24. G. Tzortzinis, C. Ai, S. F. Breña, S. Gerasimidis, Using 3D laser scanning for estimating the capacity of corroded steel bridge girders: Experiments, computations and analytical solutions, Engineering Structures 265 (2022) 114407.
25. A. J. Hart, W. Chen, H. E. Quinlan, S Gerasimidis, Feasibility of 3D Printing Applications for Highway Infrastructure Construction and Maintenance, MassDOT Report No. 22-029 (2022).
26. S. Zhang, P. Hou, J. Kang, T. Li, S. Mooraj, Y. Ren, C. H. Chen A. J. Hart, S. Gerasimidis, W. Chen, Laser additive manufacturing for infrastructure repair: A case study of a deteriorated steel bridge beam, Journal of Materials Science & Technology 154 (2023) 149–158, https://doi.org/10.1016/j.jmst.2023.01.018.
27. K.M. Zmetra, K.F. McMullen, A.E. Zaghi, K. Wille, Experimental study of UHPC repair for corrosion-damaged steel girder ends, J. Bridge Eng. 22 (8) (2017), 04017037, https://doi.org/10.1061/(ASCE)BE.1943-5592.0001067.
28. D. Kruszewski, K. Wille, A.E. Zaghi, Design considerations for headed shear studs embedded in ultra-high performance concrete as part of a novel bridge repair method, J. Constr. Steel Res. 149 (2018) 180–194, https://doi.org/10.1016/j.jcsr.2018.07.015.
29. D. Kruszewski, K. Wille, A.E. Zaghi, Push-out behavior of headed shear studs welded on thin plates and embedded in UHPC, Eng. Struct. 173 (2018) 429–441, https://doi.org/10.1016/j.engstruct.2018.07.013.
30. D. Kruszewski, A. E. Zaghi, K. Wille, Durability evaluation of headed shear studs embedded in ultrahigh-performance concrete via electrochemical corrosion, J. Bridge Eng. 24 (5). https://doi.org/10.1061/(ASCE)BE.1943-5592.0001401.
31. G. Tzortzinis, B. Knickle, S. Gerasimidis, A. Bardow, S. Brena, Identification of most common shapes and locations for beam end corrosion of steel girder bridges, in Proc., 98th Annual Meeting of the Transportation Research Board, 2019.
32. US Department of Transportation, Federal Highway Administration, National Bridge Inventory, 2019.
33. S. Bagherifard, J. Kondas, S. Monti, J. Cizek, F. Perego, O. Kovarik, F. Lukac, F. Gaertner, M. Guagliano, Tailoring cold spray additive manufacturing of steel 316 L for static and cyclic load-bearing applications, Materials & Design 203 (2021), 109575. https://doi.org/10.1016/j.matdes.2021.109575.
34. S. Yin, J. Cizek, X. Yan, R. Lupoi, Cold spray additive manufacturing and repair: Fundamentals

and applications, Additive Manufacturing 21 (2018) 628–650, https://doi.org/10.1016/j.addma.2018.04.017
35. P. Preedawiphat, N. Mahayotsanun, K. Sa-ngoen, M. Noipitak, P. Tuengsook, S. Sucharitpwatskul K. Dohda, Mechanical Investigations of ASTM A36 Welded Steels with Stainless Steel Cladding, Coatings 10 (2020), https://doi.org/10.3390/coatings10090844.
36. X. Chen, J. Li, X. Cheng, H. Wang, Z. Huang, Effect of heat treatment on microstructure, mechanical and corrosion properties of austenitic stainless steel 316L using arc additive manufacturing, Materials Science & Engineering A 715 (2018) 307–314, https://doi.org/10.1016/j.msea.2020.139514.
37. M. Liberinia, A. Astaritaa, G. Campatellib, A. Scippab, F. Montevecchib, G. Venturinib, M. Durantea, Luca Boccarussoa, Fabrizio Memola C. Minutoloa, A. Squillacea, Selection of optimal process parameters for wire arc additive manufacturing, Procedia CIRP 62 (2017), 470–474, http://creativecommons.org/licenses/by-nc-nd/4.0/.
38. M. Dinovitzer, X. Chen, J. Laliberte, X. Huang, H. Frei., Effect of wire and arc additive manufacturing (WAAM) process parameters on bead geometry and microstructure, Additive Manufacturing 26 (2019), 138–146, https://doi.org/10.1016/j.addma.2018.12.013.
39. J. H. Lee, C.M. Lee, D. H. Kim, Repair of damaged parts using wire arc additive manufacturing in machine tools, Journal of Materials Research and Technology 16 (2022): 13–24, https://doi.org/10.1016/j.jmrt.2021.11.156.
40. C. Masuo, A. Nycz, M.W. Noakes, D. Vaughan, N. Sridharan, Feasibility analysis of utilizing maraging steel in a wire arc additive process for high-strength tooling applications, Solid Freeform Fabrication 2019: Proceedings of the 30th Annual International Solid Freeform Fabrication Symposium—An Additive Manufacturing Conference, http://energy.gov/downloads/doe-public-access-plan.
41. A. Ermakova, A. Mehmanparast, Corrosion Effects on Fracture Toughness Properties of Wire Arc Additively Manufactured Low Carbon Steel Specimens, Metals 12, no. 2 (2022): 238. https://doi.org/10.3390/met12020238.
42. M. Rafieazad, M. Ghaffari, A.V. Nemani, A. Nasiri, Microstructural evolution and mechanical properties of a low-carbon low-alloy steel produced by wire arc additive manufacturing, International Journal of Advanced Manufacturing Technology 105 (2019): 2121–2134, https://doi.org/10.1007/s00170-019-04393-8.
43. L. Yang, W. Lu, Z. Liu, Y. Zhang, F. Xu, H. Gao, Z. Yao, Location-dependent microstructure and properties for plasma arc additively manufactured duplex stainless steel er2209 wire, JMEPEG 30 (2021):6788–6800, https://doi.org/10.1007/s11665-021-06005-7.
44. M. Ghaffari, A.V. Nemani, M. Rafieazad, A. Nasiri, Effect of solidification defects and haz softening on the anisotropic mechanical properties of a wire arc additive-manufactured low-carbon low-alloy steel part, JOM 71 (2019), https://doi.org/10.1007/s11837-019-03773-5.
45. J. Gea, T. Maa, W. Hana, T. Yuana, T. Jina, H. Fua, R. Xiaob, Y. Leia, J. Lina, Thermal-induced microstructural evolution and defect distribution of wire arc additive manufacturing 2Cr13 part: Numerical simulation and experimental characterization, Applied Thermal Engineering 163 (2019): 114335, https://doi.org/10.1016/j.applthermaleng.2019.114335.
46. D. Wen, P. Long, J. Li, L. Huang, Z. Zheng, Effects of linear heat input on microstructure and corrosion behavior of an austenitic stainless steel processed by wire arc additive manufacturing, Vacuum 173 (2020): 109131, https://doi.org/10.1016/j.vacuum.2019.109131.
47. H. Assadi, H. Kreye, F. Gärtner, T. Klassen., Cold spraying—A materials perspective, Acta Materialia 116 (2016): 382–407, http://doi.org/10.1016/j.actamat.2016.06.034.
48. D.M. Jafarlou, B.C. Sousa, M.A. Gleason, G. Ferguson, A.T. Nardi, D.L. Cote, I.R. Grosse, Solid-

state additive manufacturing of tantalum using high-pressure cold gas-dynamic spray, Additive Manufacturing 47 (2021): 102243, https://doi.org/10.1016/j.addma.2021.102243.
49. F.C. Lupu, C. Munteanu, B. Istrate, S.C. Lupescu, R. Ciubotaru, S. Adrian, Structural analysis and mechanical properties of some coatings obtained by cold spray method. A review, IOP Conf. Ser.: Mater. Sci. Eng. 1262 (2022): 012023, https://doi.org/10.1088/1757-899X/1262/1/012023.
50. X. Jiang, N. Overman, C. Smith, K. Ross, Microstructure, hardness and cavitation erosion resistance of different cold spray coatings on stainless steel 316 for hydropower applications, Materials Today Communications 25 (2020): 101305, https://doi.org/10.1016/j.mtcomm.2020.101305.
51. K. Spencer, M.-X. Zhang, Optimization of stainless steel cold spray coatings using mixed particle size distributions, Surface and Coatings Technology 205 (2011): 5135–5140. https://doi.org/10.1016/j.surfcoat.2011.05.020.
52. S. Yin, J. Cizekb, X. Yand, R. Lupoia., Annealing strategies for enhancing mechanical properties of additively manufactured 316L stainless steel deposited by cold spray, Surface & Coatings Technology 370 (2019): 353–361, https://doi.org/10.1016/j.surfcoat.2019.04.012.
53. T. Liao, A. Biesiekierski, C. C. Berndt, P. C. King, E. P. Ivanova, H, Thissen, P. Kingshott, Multifunctional cold spray coatings for biological and biomedical applications: A review, Progress in Surface Science 97 (2022): 100654, https://doi.org/10.1016/j.progsurf.2022.100654.
54. P. E. Carrion, N. Shamsaei., Strain-based fatigue data for Ti–6Al–4V ELI under fully-reversed and mean strain loads, Data in Brief 7 (2016): 12–15, http://doi.org/10.1016/j.dib.2016.02.014.
55. A. Fatemi, R. Molaei, Novel specimen geometries for fatigue testing of additive manufactured metals under axial, torsion, and combined axial-torsion loadings, International Journal of Fatigue 130 (2020): 105287, https://doi.org/10.1016/j.ijfatigue.2019.105287.
56. E. Irissou, J. G. Legoux, A. N. Ryabinin, B. Jodoin, C. Moreau., Review on cold spray process and technology: part I- intellectual property, Journal of Thermal Spray Technology, 17(4) (December 2008), 495–516.
57. A. Moridi, S. M. Hassani-Gangaraj, M. Guagliano, M. Dao, Cold spray coating: review of material systems and future perspectives, Surface Engineering, 36 (2014): 369–395.
58. J. Cizek, O. Kovarik, J. Siegl, K. A. Khor, I. Dlouhy, Influence of plasma and cold spray deposited Ti layers on high-cycle fatigue properties of Ti6Al4V substrates, Surface & Coatings Technology 217 (2013): 23–33, http://doi.org/10.1016/j.surfcoat.2012.11.067.
59. C. H. Boyle, S. A. Meguid, Mechanical performance of integrally bonded copper coatings for the long term disposal of used nuclear fuel, Nuclear Engineering and Design 293 (2015): 403–412, http://doi.org/10.1016/j.nucengdes.2015.08.011.
60. S. Yin , N. Fan , C. Huang , Y. Xie , C. Zhang , R. Lupoi , W Li, Towards high-strength cold spray additive manufactured metals: Methods, mechanisms, and properties, Journal of Materials Science & Technology 170 (2024): 47–64, https://doi.org/10.1016/j.jmst.2023.05.047.
61. R. F. Vaz, A. Garfias, V. Albaladejo, J. Sanchez, I. G. Cano, A review of advances in cold spray additive manufacturing, Coatings 13 (2023): 267, https://doi.org/10.3390/coatings13020267.
62. A. Gunasekaran, M. Sarhadi, Implementation of activity-based costing in manufacturing, International Journal of Production Economics 56–57 (1998): 231–242, https://doi.org/10.1016/S0925-5273(97)00139-4.
63. D. Kotoban, S. Grigoriev, A. Okunkova, A. Sova., Influence of a shape of single track on deposition efficiency of 316L stainless steel powder in cold spray, Surface and Coatings Technology, 309 (2017): 951–958, https://doi.org/10.1016/j.surfcoat.2016.10.052.
64. O.C. Ozdemir, P. Schwartz, S. Muftu, F.C. Thompson, G.A. Crawford, A.T. Nardi, V.K. Champagne Jr., C.A. Widener., High rate deposition in cold spray, Journal of Thermal Spray

Technology, 30 (2021): 344–357, https://doi.org/10.1007/s11666-020-01135-1.
65. J. Perry, P. Richer, B. Jodoin, E. Matte, Pin fin array heat sinks by cold spray additive manufacturing: economics of powder recycling, Journal of Thermal Spray Technology 28 (2019): 144–160, https://doi.org/10.1007/s11666-018-0758-3.
66. AAA, Gas Prices, accessed May 2024, https://gasprices.aaa.com/?state=MA.
67. Bureau of Labor Statistics, Occupational Employment and Wages, May 2023, "51-4121 Welders, Cutters, Solderers and Brazers," accessed May 2024, https://www.bls.gov/oes/current/oes514121.htm#st.
68. MassDOT, Transportation Innovation Conference, https://www.umasstransportationcenter.org/assnfe/ev.asp?ID=5432 (accessed May 17, 2024).
69. The American Society of Civil Engineers, Engineering Mechanics Institute Conference, https://www.emi-conference.org/ (accessed May 17, 2024).
70. National Bridge Preservation conference 2024, https://www.nbpc2024.org/ (accessed May 17, 2024).
71. National Academies, Conference on Advancing Additive Manufacturing and Construction in Transportation, https://www.nationalacademies.org/event/831_11-2024_trbs-conference-on-advancing-additive-manufacturing-and-construction-in-transportation.